Arsenic Trisulfide on Lithium Niobate for Acousto-Optic Interactions

Submitted in partial fulfillment of the requirements for

the degree of

Doctor of Philosophy

in

Department of Engineering

Md Shofiqul Islam Khan

B.Sc., EEE, Bangladesh University of Engineering and Technology (BUET)
M.Sc., Photonics, Karlsruhe Institute of Technology (KIT)

Carnegie Mellon University
Pittsburgh, PA

February, 2021

Abstract

Effective optical processing of information in the integrated photonic circuits requires strong light confinement and guiding of light at the micro-nanoscale using waveguide structures, as well as techniques to control its propagation. Optical confinement is stronger for a guiding medium with a high refractive index and complex optical information processing is possible if this refractive index can be manipulated efficiently using multiple techniques. Refractive index manipulation is possible through various methods such as electro-optic, thermo-optic, magneto-optic and acousto-optic modulation. Acousto-optic modulation technique uses strain induced by the acoustic wave to change the refractive index of the optical wave propagation medium. Such modulators have successfully been demonstrated on material platforms such as aluminum nitride, gallium arsenide and lithium niobate. Despite having some of the highest electromechanical coupling coefficients and strong acousto-optic coefficients, these material platforms cannot simultaneously exploit the best material properties because of their anisotropy. In other words, if both acoustic devices and the photonic devices are built on one of these same material platforms, both devices may not be the most efficiently optimized because of the anisotropy of the material. We have studied lithium niobate as the piezoelectric substrate which is used to generate the acoustic wave and incorporated arsenic trisulfide, an isotropic material, as the photonic material platform which enables decoupling of the acoustic device from the photonic device. We have demonstrated arsenic trisulfide on oxide on lithium niobate as a material platform for low frequency (~MHz) modulator application through an acousto-optic modulator formed by an arsenic trisulfide Mach-Zehnder interferometer, operating in a push-pull configuration and placed inside a surface acoustic wave cavity on a Y-cut lithium niobate wafer. A comprehensive analytical modeling of the acousto-optic interaction is offered which enabled the first ever extraction of acousto-optic coefficients for the thin film arsenic trisulfide from an integrated device. First ever extraction of the thermal coefficients for waveguides on arsenic trisulfide, lithium niobate on insulator and arsenic trisulfide on lithium niobate on insulator using optical racetrack resonators is also demonstrated. Arsenic trisulfide on lithium niobate on insulator is discussed as a high frequency (~GHz) modulator platform which includes a qualitative study of this hybrid material platform. This hybrid material platform will pave new opportunities for microwave-to-optical conversion, non-reciprocal devices, Brillouin scattering and beam steering applications.

Dedication

To My Parents and Poochi……

Acknowledgements

I place on record, my sincere gratitude to my supervisors, Professor Gianluca Piazza and Professor James A. Bain, with whom my pursue for the doctoral degree has been a vivid journey. Their constant support and guidance have helped me learn about research methods, critical thinking, research ethics and technical skills development. They have equally contributed in my personal and professional skill development, and I feel honored that I had the opportunity to work with them. I have observed some of their unique qualities that I plan to cherish for the rest of my life.

I am grateful to Professor Maysam Chamanzar and Dr. Radwanul Hasan Siddique for serving in my prospectus and thesis defense committee. Their feedback and recommendations have provided significant guidance to my research quest.

I am thankful to my past and present research group members and office colleagues who have contributed enormously in my professional and personal development. I would love to name few of those group members, Gabriel, Mohamed, Abhay, Jitendra, James, Emad, Lutong, Ashraf, Luca, Zach, Pietro, Ayaz, Zia, Xinyi and colleagues Jay, Zabir, Darshil, Abir, Zia, Phoebe and Arman. I am highly indebted to the entire staff of the Claire & John Bertucci Nanotechnology Laboratory: Matt, Mason, Norman, James, Dante and Mark without whom this research endeavor could become more challenging.

I am also grateful to my parents, my family and friends for their constant support and encouragement throughout this long journey. I am also blessed to have a great community life in Pittsburgh because of a wonderful bunch of friends and caring people, if I start naming them here, it would surpass the original size of this document. But I must mention my best friend Suchi, who have taught me to be a better and stronger person. Along with my parents, I am dedicating this document to her as well, the least I could offer to honor her contributions in my life.

This work was funded in the framework of the PRIGM-AIMS Project by the Defense Advanced Research Projects Agency (DARPA) under Award No. N66001-16-1-4025.

Contents

List of Figures

Chapter 1

Introduction

Integrated photonic platforms exploit various techniques to manipulate light propagation through optical waveguides such as electro-optic (EO) [1, 2], magneto-optic [3], carrier injection [4] or thermo-optic [5] modulation. Another versatile technique to control the refractive index profile of an optical propagation medium is to harness interaction between acoustic and light waves. This approach has been successfully demonstrated in different thin films such as lithium niobate (LN) [6], aluminium nitride (AlN) [7] and gallium arsenide (GaAs) [8]. Although LN and GaAs have some of the highest electromechanical (EM) coupling coefficients and acousto-optic (AO) coefficients, AO devices made on these platforms cannot simultaneously exploit the best material properties. These materials are single crystalline and anisotropic, which means EM and AO coefficients are functions of the specific direction of operation. Because of their anisotropy, it is hard to co-fabricate optical and acoustic devices that simultaneously exhibit maximum EM and AO characteristics. As_2S_3, a chalcogenide glass, offers both a high AO coefficient and a high refractive index [9], hence making it a promising candidate for AO interactions. The prime advantage of using As_2S_3 on LN is that the As_2S_3 film is isotropic and therefore decouples the orientation of the acoustic transducer with respect to the photonic component [10] making it an excellent candidate for heterogeneously integrated [11] AO devices [6]. Our objective is to demonstrate the full potential of As_2S_3 on LN platform, successful engineering of which would allow EM, EO and AO interactions all-in-one platform. To investigate the full potential of As_2S_3 with LN, we are primarily focused on two material stacks:

- As_2S_3 on oxide on LN substrate
- As_2S_3 on Lithium Niobate on Insulator (LNOI)

Fig. 1.1 shows a high level schematic of an acousto-optic modulator (AOM), which has two major parts: the acoustic device and the photonic readout. On the acoustic device part, interdigitated transducers (IDTs) are used to generate acoustic waves on the piezoelectric material (i.e. LN). Propagation of the acoustic wave creates strain on the material platform which can be detected using photonic circuit in As_2S_3. Optical signals at the two arms of the mach-zehnder interferometer (MZI) are modulated by the strain induced optical phase change which can be combined and detected as amplitude modulation using photodetector. Key tasks to be performed to build such AOM can be listed as follows:

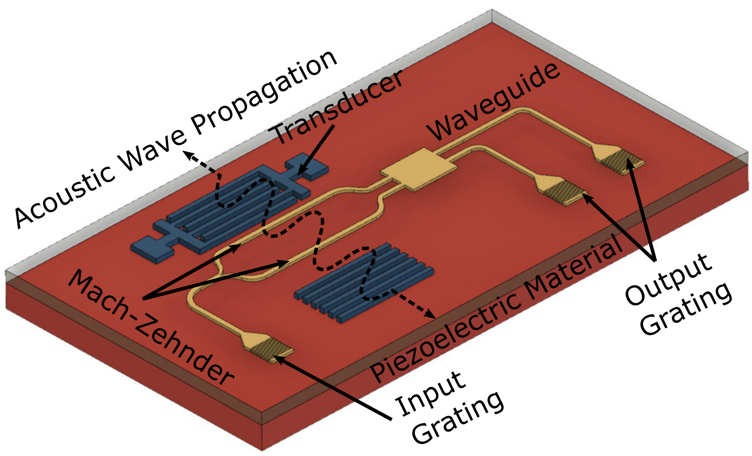

FIGURE 1.1: Schematic of the acousto-optic modulator with transducer to generate acoustic wave and Mach-Zehnder interferometer as the photonic detection circuit.

- Explore photonic components
  - Devise efficient light injection technique using grating coupler
  - Characterize material properties using photonic resonators: propagation loss, extraction of thermo-optic properties etc.
- Explore acoustic device design
- Integrate acoustic and photonic devices
- Explore acousto-optic properties of the material system

Acoustic devices on bulk LN were developed as part of the AO gyroscope application [6]. These devices were used to explore AO interactions in As_2S_3 on oxide on LN platform. Because of the large acoustic wavelength used in this application, it was possible to achieve AO interactions in a waveguide made exclusively out of As_2S_3. Gyroscope application motivated the development of the first material platform.

In contrast, for high frequency (HF) applications, the acoustic wavelength becomes comparable to the oxide and As_2S_3 layer thicknesses. Therefore, to achieve efficient AO interactions, As_2S_3 is directly deposited on LNOI. As a material system, As_2S_3 offers 4x stronger modulation strength over thin films of LN. By putting As_2S_3 directly on top of LNOI, a hybrid acousto-optic platform can be demonstrated, which will enable electromechanical, electro-optic and acousto-optic modulation simultaneously in the same platform at high frequency (~GHz). The HF application motivates the development of the second material platform.

By integrating As_2S_3 with both bulk LN and LNOI platform, this thesis work would make the following contributions in advancing the state-of-the-art:

- Demonstration of thin film As_2S_3 as a promising acousto-optic material system with one of the highest AO coefficients reported in the literature
- Decoupling of acoustic and photonic device design constraints in an acousto-optic modulator
- Comprehensive analytical modeling of AO interaction in As_2S_3 on oxide on LN platform and first ever extraction of AO coefficients for thin film As_2S_3 from an integrated device
- First ever extraction of thermal coefficients (including both thermo-optic and thermal expansion effect) for As_2S_3, LNOI and As_2S_3-LN hybrid waveguide using optical racetrack resonators which shows that thermal expansion has a dominant effect on As_2S_3
- Qualitative study of the high frequency AO platform with As_2S_3 on LNOI paving new opportunities for microwave-to-optical conversion [12], non-reciprocal devices [13], Brillouin scattering [14] and beam steering applications

This thesis work summarizes the advancements made to date in demonstrating these two material platforms and proposes a path to the demonstration of the HF AOM. A summary of the thesis structure is presented in the following table:

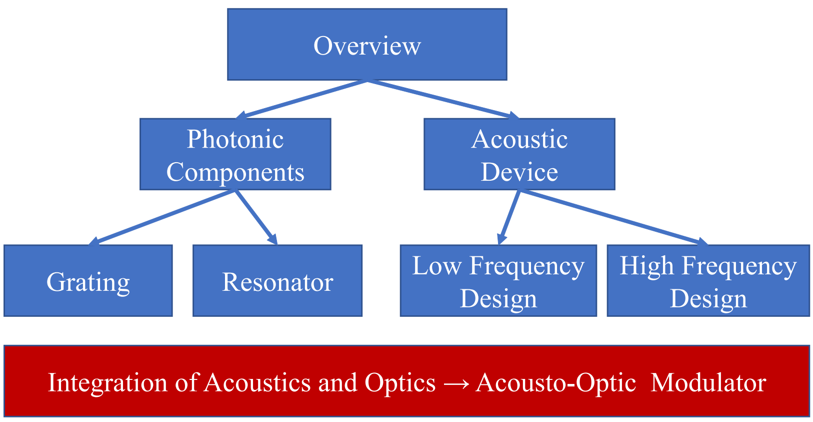

First a general overview on the fabrication process is presented. Then the design and characterization of the photonic components in these two material platforms are thoroughly discussed. Afterwards, the acoustic devices are studied. Finally, integration of acoustic and photonic components for the demonstration of AOM is analyzed.

Chapter 2

Fabrication Process

Fabrication processes are developed for the integration of As_2S_3 with both bulk LN substrate and LNOI (where the substrate is either LN or silicon). In this chapter fabrication challenges associated with the processing of As_2S_3 is described. Later, a general overview of the fabrication process flow for AOM development in both material platforms are illustrated.

2.1 Challenges and Remedy

The fabrication process for As_2S_3 is not straightforward, as it is sensitive to the visible light illumination which induces photo-oxidation of the film surface in an ambient atmosphere [15] which in turn produces micron-sized As_2O_3 crystallites that are clearly visible in fig. 2.1(a). Surface roughness caused by these crystallites may result in significant optical propagation loss. Besides, As_2S_3 dissolves in alkaline photoresist [16], making it harder to pattern with photolithography or process it for an integrated device, which may include photolithography in its fabrication steps. We have taken these into account while developing fabrication process to integrate As_2S_3 with LN. Our experimental approach demonstrated (in fig.2.1(b)) that passivation with silicon dioxide (~ 80 nm) assures As_2S_3 is protected from degradation when exposed to ambient condition.

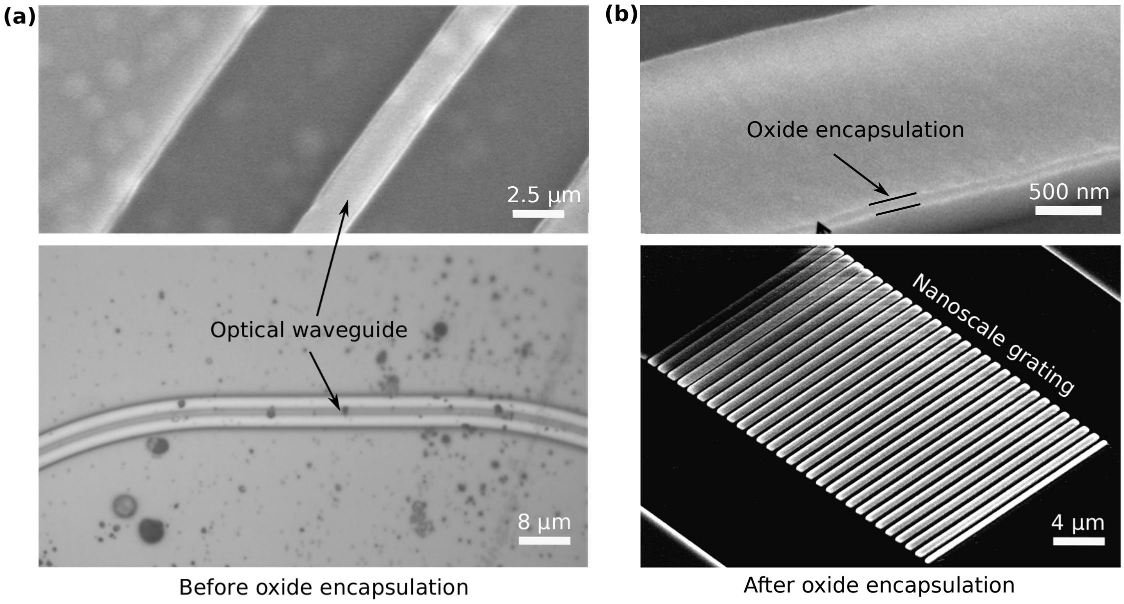

Figure 2.1: Effect of oxide encapsulation: (a) samples without encapsualtion and (b) samples with oxide encapsulation.

2.2 As_2S_3 on Lithium Niobate (LN)

The microfabrication process for the making of the AOM device using As_2S_3 on oxide on LN platform is depicted in fig. 2.2 in several steps. Starting with LN substrate (step 1), tungsten was chosen as the metal for the electrodes and a 600 nm thick layer was lifted off to form the IDTs, reflectors and pads on a 4" Y-cut LN wafer (step 2). The choice of materials and design parameters were dictated by the specific-end application, an acousto-optic gyroscope[17], which requires the metal layer to provide for the following: high mass density to synthesize a large Coriolis mass, high acoustic reflection to minimize energy leakage from the cavity and low thermo-elastic damping to minimize acoustic losses [18]. Aluminum has low mass density, gold suffers from thermo-elastic damping, whereas tungsten can attain all three desired characteristics. Besides, processing thick (~600 nm) gold film is difficult compared to tungsten. For these various reasons, tungsten was preferred

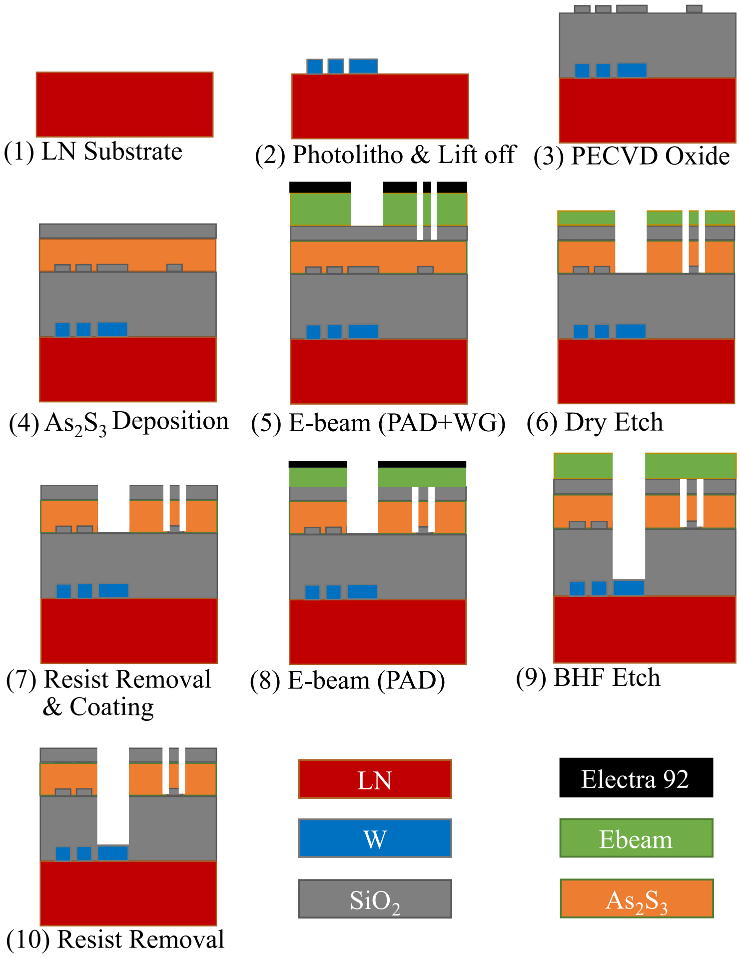

FIGURE 2.2: Fabrication process for AOM on As_2S_3 on oxide on LN.

over gold or aluminum. A 1.6 μm thick oxide cladding layer was deposited using plasma-enhanced chemical vapor deposition (PECVD) technique (step 3) followed by a 330 nm magnetron sputtering of As_2S_3 (step 4). The oxide cladding thickness was selected in such a way that the light reflected back from the oxide-LN interface constructively interferes with the light in the grating coupler, hence maximizing light coupling in the As_2S_3 without compromising acoustic energy coupling in the same layer [19]. To prevent As_2S_3 photo-decomposition by exposure to ambient oxygen, a thin (35 nm) capping oxide layer was sputter-deposited without breaking vacuum on top of As_2S_3 [16]. Elionix ELS-G100 Electron Beam Lithography System was used to define optical waveguides and the pad locations in electron-beam resist, CSAR 62, and transfer them to As_2S_3 (step 5). Electra 92, a water-soluble conductive layer, which helps to reduce the charging issues during e-beam exposure, was also used. The thin oxide cap layer and As_2S_3 were dry etched using Cl_2 and BCl_3 gases in a Plasma Therm Versaline Inductively Coupled Plasma (ICP) etcher (step 6). In this Chlorine etch process, etch rates of 3.5 nm/s for resist, 1.3 nm/s for oxide and 40 nm/s for As_2S_3 were recorded. After the etch process, remaining resists are removed and a oxide cap layer is sputter deposited to cover the open As_2S_3 waveguide sidewalls (step 7).

Concentrated hydrofluoric (49% HF) acid was used to wet etch the cladding oxide. As_2S_3 acted as a hard mask in the concentrated HF enabling the definition of pad openings (step 9). A second capping oxide thin film was sputter deposited, immediately after the As_2S_3 etch for pad opening step. This was required since concentrated HF use removes the first cap oxide layer while etching the bottom oxide. Afterwards, another e-beam lithography step was used to pattern the MZI, MMI and grating couplers in As_2S_3. A final cap oxide thin film was sputtered to cover the waveguide sidewalls, after etching As_2S_3 for photonic circuit patterning. A third e-beam lithography step was done for final pad opening and BHF wet etch was used to remove remaining oxide thin film from the pad areas. It is important to note that the necessity to perform the pad opening step in multiple stages was dictated by the requirement to ensure electrical contacts to the electrodes, while minimizing the risk of photo-decomposition of As_2S_3.

2.3 As_2S_3 on Lithium Niobate on Insulator (LNOI)

AOM device fabrication process on As_2S_3 on LNOI is summarized in fig. 2.3. Aluminum is chosen as the electrode metal, 150 nm of which was deposited using e-beam evaporation technique.

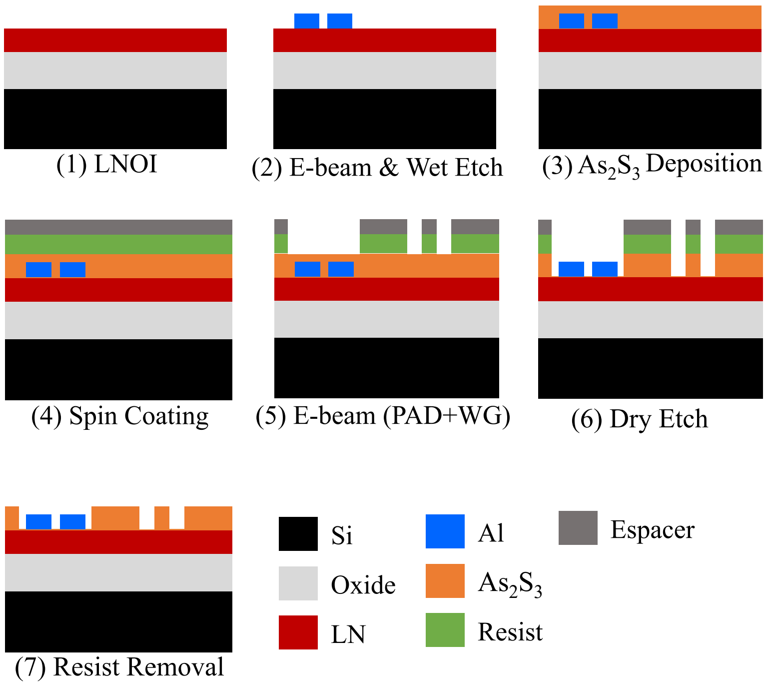

FIGURE 2.3: Fabrication process for AOM on As_2S_3 on LNOI.

Negative e-beam resist HSQ was used for patterning the interdigitated transducer (IDT) structure and AZ 400K developer was used for etching Al. Later 270 nm of As_2S_3 was sputter deposited using magnetron sputtering method. CSAR and Electra 92 were used as e-beam resist and conductive layer respectively, to pattern photonic circuit and opening PAD areas for making electrical probing possible. As_2S_3 was etched using ICP reactive ion etching (RIE) technique and Cl_2 chemistry.

Chapter 3

Photonic Components

Successful integration of an acousto-optic modulator would require carefully designed photonic components as well as acoustic devices. In this chapter, we discuss different photonic components that we have designed, fabricated and tested. These photonic components were required either as the building blocks for the modulator device, or to characterize material properties which are relevant for the modulator device performance.

3.1 Grating Couplers

3.1.1 As_2S_3 on LN

A challenge for the demonstration of this hybrid material platform is efficient light injection into a photonic waveguide using standard coupling techniques like vertical grating couplers [20], which have become a mainstream method for light coupling in Si photonic applications. Beside tapered coupling in hybrid integrated system using silicon and As_2S_3 [21], the best reported As_2S_3 on LN grating coupler offers -3.75 dB of coupling efficiency (CE), but uses complex bragg reflector mirrors and attains minimum CE only at a coupling angle of 17^0 [22]. Vertical coupling is a preferred method to couple light from either fibers or heterogeneously integrated laser sources, but its use dramatically degrades injection efficiency due to back reflections [23, 24]. One of the major causes behind back reflections is the second order reflection of the grating coupler. We demonstrated a simple fabrication process to incorporate As_2S_3 on LN with efficient light injection technique using chirped vertically coupled gratings with an aluminium (Al) reflector mirror at the interface between silicon dioxide (SiO_2) and LN (fig. 3.1(a)). The efficiency enhancement by chirping and the introduction of a mirror are inspired by progress made by the silicon photonic industry. [25].

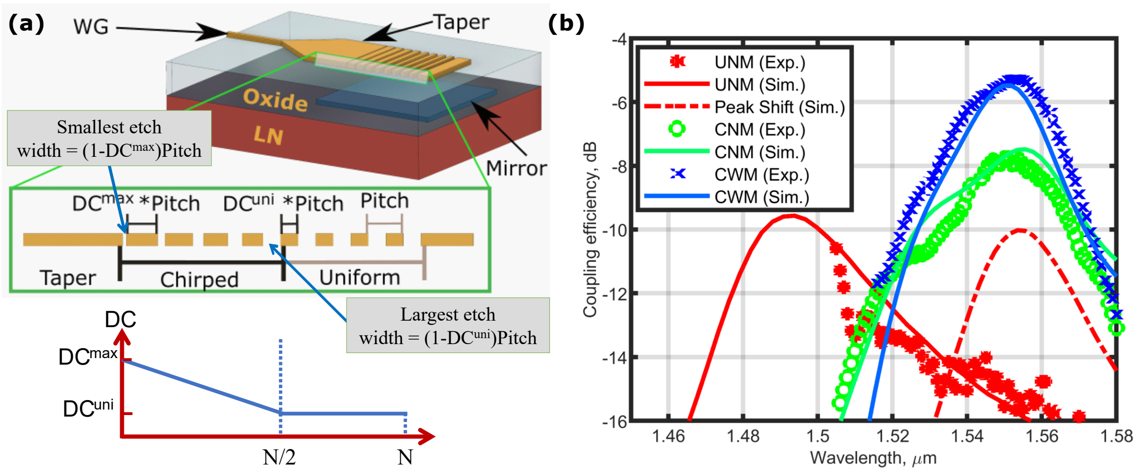

Figure 3.1: (a) Grating coupler on As_2S_3 on oxide on LN. (b) Effect of chirping and metal mirror on grating coupler coupling efficiency demonstrated through simulation and experimental data. Here, UNM = uniform with no mirror, CNM = chirped with no mirror, and CWM = chirped with metal mirror. Grating parameters are: Λ_0 = 935 nm, DC^{uni} = 0.76, DC^{max} = 0.92. Peak Shift = coupling efficiency for UNM when the pitch is adjusted in simulation to a different value (975 nm) to center its response around 1550 nm.

Fig. 3.1(a), shows the schematic of a 1D grating coupler with an adiabatic taper. We selected a 1D grating coupler with 30 grating cells (each cell having a fully etched and an un-etched portion of As_2S_3) and a width of 17 μm, which is larger than the fiber mode to avoid scattering at the edges of the grating waveguide. To convert the mode shape of the optical signal from the fiber and match it to the 1.5 μm x 0.33 μm wire waveguides, we selected a 700μm long adiabatic taper. Since our goal was to extract the grating coupler coupling efficiency, the wire waveguides were made as short as possible (~ 300 μm) to minimize the impact of propagation losses on the grating loss extraction. In the chirped grating coupler design, only half of the grating cells were chirped while the other half was kept uniform. Starting from the taper end where the grating cells begin (fig. 3.1(a)), the first 15 grating cells were chirped. The duty cycle (DC = un-etched width of grating cell/pitch) of the first grating cell at the taper end was set to DC^{max}, while the 15^{th} cell had the same DC as that of the uniform portion: DC^{uni}. The DC of the chirped cells (DC_i^{chirp}) were linearly varied starting from DC^{max} to DC^{uni} where i represents the grating cell index. Starting from the taper end, DC variation can be expressed by the following equation:

$$DC_i^{chirp} = (i-1)\frac{DC^{uni} - DC^{max}}{N/2-1} + DC^{max} \tag{3.1}$$

For a pitch of Λ_0 of the grating, the size of the smallest etched width is $\Lambda_0(1-DC^{max})$, whereas the size of the etch in the uniform portion of the grating is $\Lambda_0(1-DC^{uni})$. The rest of the 15 cells were kept as uniform grating cells with a DC of DC^{uni}.

The purpose of cascading a uniform grating after the chirped portion was to enhance back reflection into the chirped portion and steer light vertically. Our simulations confirmed that splitting equally the grating cells between uniform and chirped was sufficient to minimize back reflections. The chirped grating design was performed using Lumerical FDTD commercial simulation tool. The design procedure consisted in first identifying optimal uniform and fully etched gratings without reflectors using 2D FDTD simulations. Once an optimal pitch and DC were determined, then chirped gratings were designed. The parameters of the uniform portion of the chirped grating were kept the same as those that were optimized for the fully uniform grating. For the chirped portion, the pitch was left unchanged, whereas the DC was linearly varied between the value used for uniform gratings (DC^{uni}) and a maximum value (DC^{max}). To find an optimal design for the chirped grating this DC^{max} was varied between DC^{uni} and 92-94%. The choice of maximum value of DC^{max}, was constrained by the minimum etch width achievable through the fabrication. The minimum etch width achieved in our fabrication process was ~ 50 nm.

It is important to note that in order to identify the optimal DC for both set of simulations (uniform and chirped gratings) a brute force approach was used. The grating response was simulated over a broad optical wavelength (1400 nm to 1600 nm) for a fixed pitch as the DC was swept. Once an optimal DC was found at a particular wavelength, the pitch of the grating coupler was refined so that the response would be centered at 1550nm. The results of this analysis revealed that a chirped grating consisting of a pitch of 940 nm, DC^{max} of 94% and DC^{uni} of 78% accompanied by an Al reflector mirror would demonstrate a maximum achievable coupling efficiency of 3 dB, assuming no fabrication imperfections. Practically fabrication process bias and imperfections make it difficult to attain the exact design dimensions. Therefore, we have fabricated multiple sets of devices varying the pitch and duty cycle in order to achieve our desired design parameters. Some of these device geometries are considered to serve two purposes. First to showcase the effect of chirping and the use of metal mirror on CE, and second to achieve the best possible CE. After measuring the fabricated devices, we selected a subset which helped making our point about the impact of chirping and the Al reflector. We only reported the 3D FDTD simulation results for those structures to further confirm their agreement to the experimental values.

In fig. 3.1(b), we report the experimental measurements for a particular type of fabricated devices with the following parameters: Λ_0 = 935 nm, DC^{uni} = 0.76, DC^{max} = 0.92. The response of this device is plotted to demonstrate that for similar structural parameters, chirping improves CE by 7 dB with respect to the uniform grating and that the Al mirror provides for an additional 2.3 dB of CE improvement with respect to the chirped grating at the wavelength of 1550 nm. The experimental results are in agreement with the simulations. Simulation result reveals that the peak coupling efficiency for this uniform grating is located at a shorter wavelength and beyond the operation range of the source used for measurement. However, by increasing the pitch of the grating, the peak of CE can be pushed around 1550 nm without resulting in a significant change (~ 1 dB) to the magnitude of the maximum CE. When compared to this simulated value, chirping improves CE by about 2 dB with respect to UNM. An uncertainty exists in the extraction of the index of refraction of the As_2S_3 film, which was done using a Rudolph ellipsometer. The value of the index of refraction of As_2S_3 can only be bound to be between 2.35 and 2.43 and 2.35 was used as a fitting parameter in the simulations. Nonetheless, some discrepancies between simulation and experimental data still exists and can be attributed to fabrication imperfections.

The best grating coupler measured is a chirped structure with metal mirror, which demonstrates 4 dB coupling efficiency with 3 dB bandwidth of 40 nm at the wavelength of 1550 nm (fig. 3.1(b)). Simulation results reveal that when the guided mode reaches the grating, a portion of light is

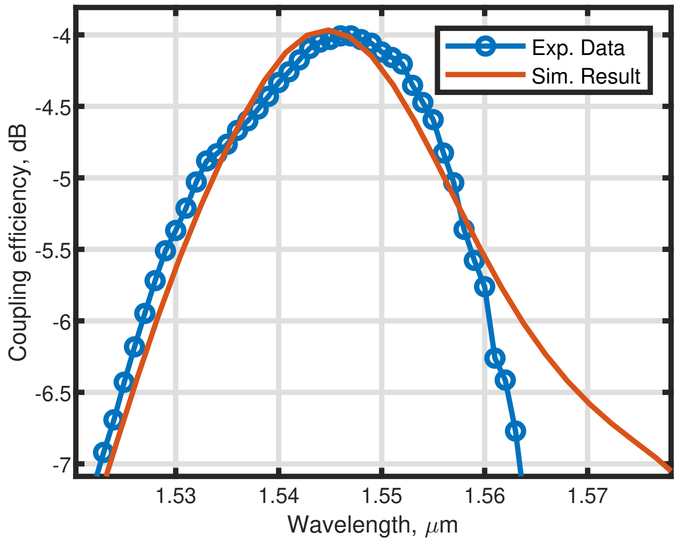

Figure 3.2: Comparison of measurement results with simulations for the best fabricated As_2S_3 vertical grating couplers on LN. Grating parameters for this device are: Λ_0 = 945 nm, DC^{uni} = 0.77, DC^{max} = 0.91

reflected from the grating region, a portion is diffracted upwards, another goes downwards and reflects back from the mirror. Due to chirping, reflected and transmitted portions of the light are negligible. Most of the light is scattered upwards, which is enhanced by the reflection from the metal mirror, but only a portion of it matches the fiber mode which is detected through the photodetector. Further enhancement of the coupling efficiency may be possible by designing the grating parameters ensuring phase matching conditions (apodization process) in order to achieve stronger overlap between the diffracted and the fiber mode. Besides, waveguide grating width may be tuned to ensure best performance [26]. The grating parameters for the best measured device are: Λ_0 = 945 nm, DC^{uni} = 0.77, DC^{max} = 0.91. Our 3D FDTD simulations are overlapped with the experimental results and exhibit a very good agreement except for the behavior beyond 1560 nm. At this time we are unsure about the sources of this discrepancy. It was not possible to achieve the 3 dB coupling efficiency predicted by the simulations due to fabrication imperfections.

3.1.2 As_2S_3 on LNOI

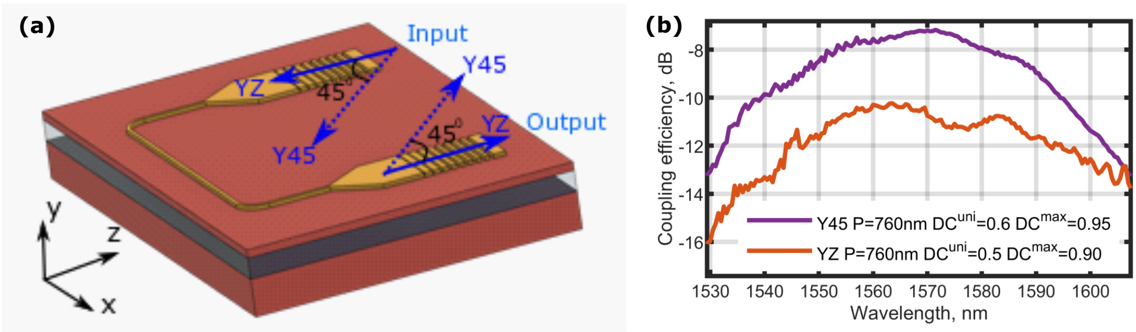

FIGURE 3.3: (a) Grating coupler on As_2S_3 on LNOI. (b) measurement data.

By putting As_2S_3 directly on top of LNOI, a hybrid acousto-optic platform can be demonstrated which may enable electromechanical, electro-optic and acousto-optic modulation simultaneously in the same platform. Such hybrid platform is necessary for high frequency (~GHz) application as the acoustic wavelength is comparable to the bottom cladding oxide. Fig.3.3(a) shows a schematic of the input-output As_2S_3 grating coupler connected via a 2μm wide hybrid As_2S_3-LN wire waveguide. Fig.3.3(b) shows experimental measurement of grating coupler efficiency on Y-cut LNOI wafer for light injection direction along z-axis (YZ orientation) and light injection direction 45^0 rotated about the y-axis (Y45 orientation) to be -10.7 dB and -7.2 dB respectively. These were chirped 1D gratings with a pitch of 760 nm. Half of the grating cells were chirped starting with DC^{max} = 0.90 and the following cells with linearly decreasing DC up to the uniform grating cells with DC^{uni}= 0.5 for YZ gratings. In case of the Y45 grating fill factors were DC^{max} = 0.95 and DC^{uni} = 0.6.

3.2 Optical Waveguides

Optical waveguides are key components for light transportation on-chip as well as acousto-optic interaction. Based on the specific requirements, we have designed and fabricated optical waveguides by etching trenches in As_2S_3 thin film. Fig. 3.4 shows schematic of waveguides on both As_2S_3 and As_2S_3-LN hybrid platform. As in fig. 3.4(a), As_2S_3 is the core material where oxide acts as the bottom cladding and air as the top cladding layer. Fig. 3.4(b) shows hybrid waveguide where propagating mode is shared within the As_2S_3-LN hybrid core, 40% in As_2S_3 and 55% in LN thin film for a waveguide dimension of 1.7 x 0.27μm.

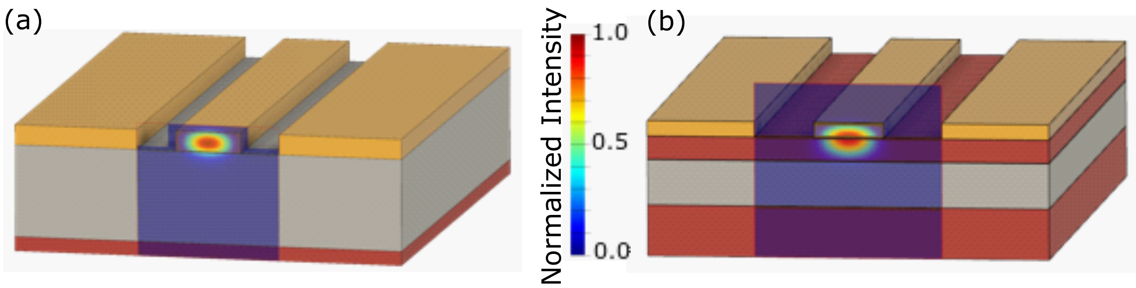

FIGURE 3.4: Normalized electric field intensity in (a) As_2S_3 waveguide and (b) As_2S_3-LN hybrid waveguide, obtained from Lumerical finite difference eigenmode solver. In the experiment, a 3 μm wide trench is etched on either side of the wire waveguide.

3.3 Optical Resonator: Propagation Loss

In general, all pass optical ring resonator consists of a looped optical waveguide along with a bus waveguide to access the loop using coupling mechanism (grating couplers in our case). When the optical wave inside the loop accumulates a round trip phase shift which is an integer multiple of 2π (3.5(a)), the waves interfere constructively and the cavity is in resonance. In racetrack resonators (RTs), the total length (L_t) of the loop is determined by two arcs and two parallel straight waveguides, $L_t = 2L + 2\pi R$ (fig. 3.5(c)). While in resonance, we can measure the optical Q-factors of the RT with different straight section lengths keeping the bend radius constant and extract propagation loss for straight waveguides.

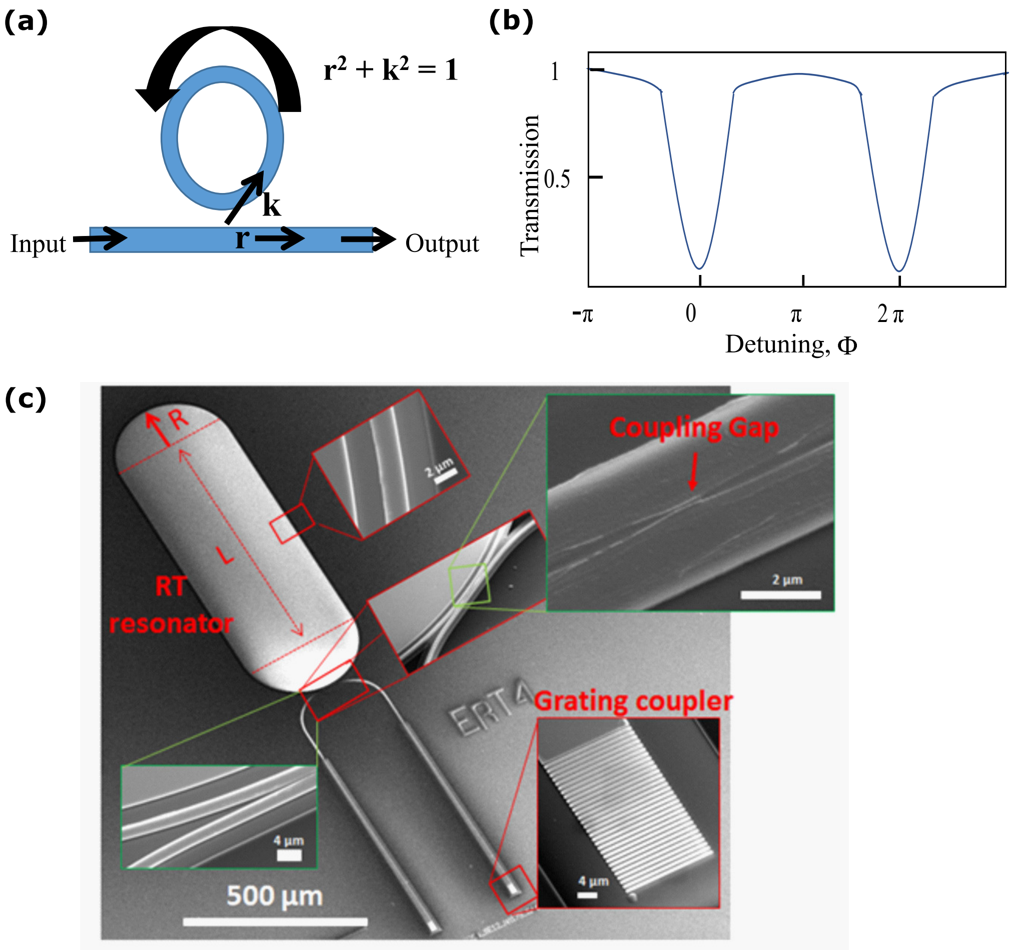

Figure 3.5: Optical resonator: (a) self and cross coupling coefficient, (b) schematic of transmission through a waveguide coupled to a resonator and (c) SEM images of optical racetrack resonator device for propagation loss extraction.

The transmission characteristic of resonators (fig.3.5(b)) depends on the single-pass amplitude transmission (a) and self-coupling coefficient (r) of the resonator as follows [27]:

$$T = \frac{a^2 - 2racos\phi + r^2}{1 - 2racos\phi + (ra)^2} \longrightarrow \frac{(a-r)^2}{(1-ra)^2} \tag{3.2}$$

where $\phi = \beta L_t$ ($= 2m\pi$ at resonance and $m =$ 1,2,...) is the single pass phase shift and β is the propagation constant of the circulating mode. Both propagation loss in the ring and coupler are included in a which relates to the attenuation coefficient α $[cm^{-1}]$ as $a^2 = exp(-\alpha L_t)$. By measuring the transmission spectra of the racetrack resonator, the loaded Q-factor of the resonator can be extracted which allows solving for a and r as Q factor is expressed as:

$$Q = \frac{\lambda}{FWHM} = \frac{2\pi n_{eff} L}{2\lambda cos^{-1}(\frac{2ra}{1+(ra)^2})} \tag{3.3}$$

Here, n_{eff} is the effective index of the waveguide medium. By comparing total losses from different length waveguides, the loss per unit length of the straight waveguide can be evaluated. In fig. 3.6(a), RT resonators with access waveguide are demonstrated. The access waveguide has input and output grating couplers. Light from a TSL-550 tunable laser source can be fed through a vertical groove array (VGA) holding a fiber and an on-chip grating coupler. Similarly, diffracted light from output grating captured through a VGA port and can be detected by a photodetector (PD).

Experimental results show that 330 nm thick As_2S_3 waveguide with 2.5 µm width has a propagation loss of 4.4 dB/cm and waveguide with 3.5 µm width has a propagation loss of 5.4 dB/cm (fig. 3.6(a)). These losses are acceptable for our desired application. In case of the hybrid waveguide (fig. 3.6(b)), propagation loss for YZ resonators is 0.54 dB/cm and Y45 is 1.86 dB/cm. We believe that higher propagation loss in Y45 resonators than YZ can be attributed to the scattering at the waveguide edges due to surface roughness

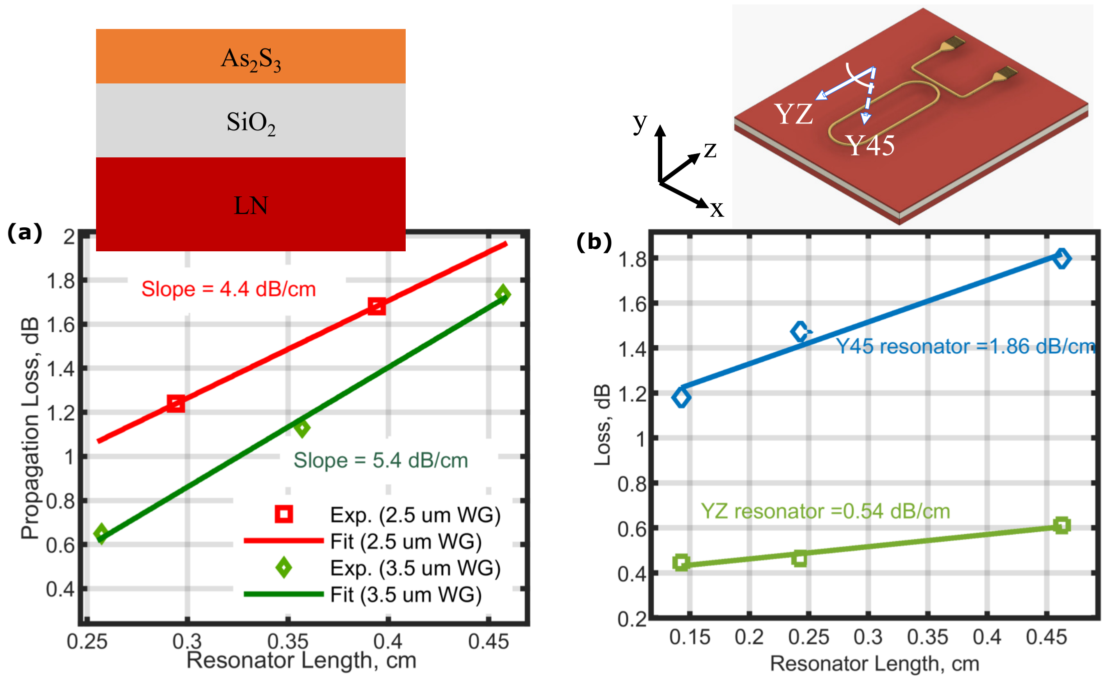

Figure 3.6: (a) Propagation loss from the 2.5 μm and 2.5 μm wide As_2S_3 waveguide and (b) propagation loss from the 2 μm wide As_2S_3-LNOI hybrid waveguide for racetrack orientation in YZ and Y45.

originated from the lithography process. Overall propagation loss is lower in case of the hybrid waveguide, which could be because of an additional sonication step added during the resist removal. SEM imaging confirms that the waveguide surface quality is cleaner for the samples going through the sonication step for resist removal.

3.4 Optical Resonator: Thermal Properties

Photonic properties of the modulated signal is sensitive to temperature variations. In the hybrid As_2S_3-LNOI platform the propagating optical mode is distributed between both material systems. Therefore, the thermo-optic coefficients of both materials will contribute to the resultant thermo-optic coefficient of the hybrid material platform. To fully identify the contribution from both material, their individual thermo-optic coefficient needs to be extracted as well as for the hybrid platform.

3.4.1 Theoretical Analysis

Optical racetrack resonator (RTR) is useful in extracting thermo-optic coefficient of the material systems. Resonant wavelength of the RTR can be expressed as follows:

$$\lambda_0 = \frac{n_{eff0} L_0}{m}, m = 1, 2, 3.... \tag{3.4}$$

where, at temperature T_0, λ_0 is the wavelength for the resonant condition, for a total RT length of L_0. For a temperature of T, effective index changes by $\frac{dn}{dT}(T - T_0)$ and RT length changes by $\frac{dL}{dT}(T - T_0)$ which is determined by the thermo-optic ($\frac{dn}{dT}$) and thermal expansion coefficient ($\frac{dL}{dT}$) of the material system. Resonant peak shift depending on the temperature variation can be determined by:

$$\frac{\lambda_T - \lambda_0}{\lambda_0} = (\frac{dn}{dT} + \frac{dL}{dT})(T - T_0) \tag{3.5}$$

Here, T_0 is any reference temperature and T is the temperature of interest. Using this principle we have extracted thermal coefficient ($\alpha_T = \frac{dn}{dT} + \frac{dL}{dT}$) for nanophotonic waveguide medium on LNOI, As_2S_3 on LNOI and As_2S_3 on bulk LN platform. This extraction is based on the assumption that $\frac{dn}{dT} . \frac{dL}{dT} (\Delta T)^2 \approx 0$

3.4.2 Experimental Setup and Measurement

Experimental setup for extracting thermal properties is demonstrated in fig. 3.7(a), which consists of a tunable laser source (1500 - 1630 nm), photodetector (power meter), polarizer, thermo-couple reader, hotplate and vertical grooved array (VGA) for fiber-to-chip light coupling. The device under test (DUT) is placed on the hotplate and the sample temperature is read from both the thermo-couple reader (connected to the DUT surface using carbon tape) and the hotplate reader.

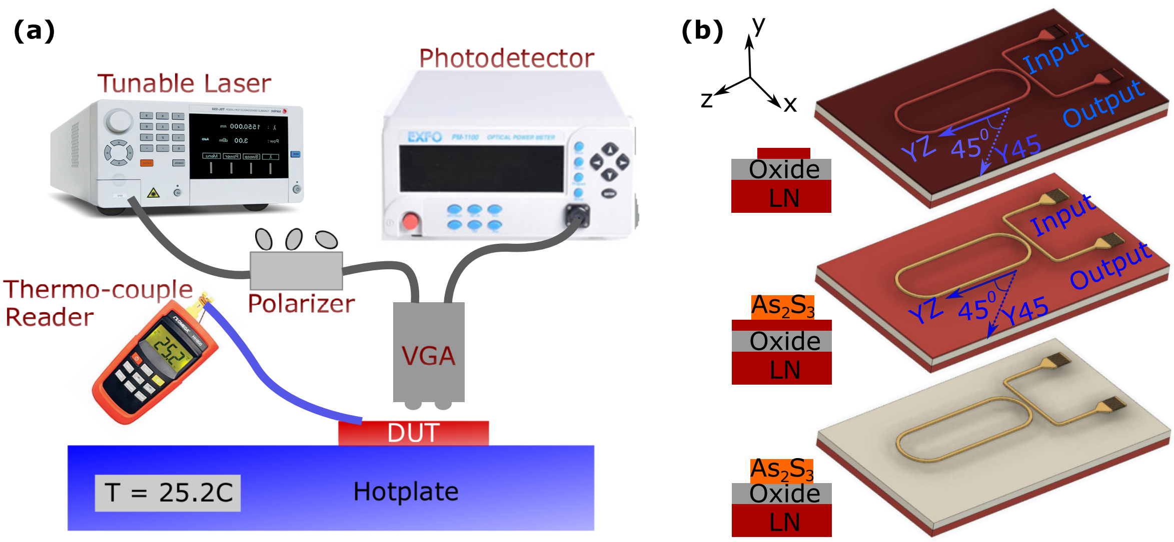

FIGURE 3.7: (a) Experimental setup for thermal coefficient extraction. (b) Different photonic waveguide mediums which are under thermal coefficient study.

To study the thermal coefficient (α_T) we have considered three different waveguide media which are depicted in fig. 3.7(b). Y-cut LN is chosen as the material platform, and As_2S_3 is incorporated with either bulk LN or LNOI. For light injection or light propagation in the parallel arm of RT, YZ and Y45 direction are chosen in this study. The following table summarizes the properties of the DUTs:

Table 3.1: Summary of the Waveguides (WGs) for α_T Extraction

Platform	LNOI	LNOI	As_2S_3-LNOI	As_2S_3-LNOI	As_2S_3
Orientation	YZ	Y45	YZ	Y45	Isotropic
WG Type	Rib	Rib	Rib	Rib	Ridge
WG Dimension (μm)	2x0.3	2x0.3	1.7x0.27	1.7x0.27	1.5x0.33

Fig. 3.8(a) shows an example of RT transmission spectrum. Transmission spectra were measured at different temperatures using the hotplate setup. Choosing one of the resonant dips as a reference (λ_0) and a temperature as reference temperature (T_0), α_T can be extracted using eqn. 3.5. For statistical purposes, the measurements were repeated by ramping temperature up, ramping down and then ramping up again. This method also ensures that there is no hysteresis associated with the temperature increasing or decreasing. The extraction of α_T for various material platforms and orientations are demonstrated in fig. 3.8(b-f). Extracted thermal coefficients are represented with a 95% confidence bound. A table is presented below to summarize the experimental results. Such thermal parameter extraction was performed for the first time on these thin film material platforms.

Table 3.2: Tabulation of α_T for Various Platforms

Platform	LNOI	LNOI	As_2S_3-LNOI	As_2S_3-LNOI	As_2S_3
Orientation	YZ	Y45	YZ	Y45	Isotropic
α_T, ppm/K	11	18	63	87	155
Literature (dn/dT) ppm/K[28]	4.4 (LN)	4-37 (LN)	4.4 (LN) 17 (As_2S_3)	4.4-37 (LN) 17 (As_2S_3)	17
Literature (dL/dT) ppm/K [29]	4.1 (LN)	4-15 (LN)	4.1 (LN) 150 (As_2S_3)	4.4-37 (LN) 150 (As_2S_3)	150

For YZ orientation, α_T demonstrates alsmost equal contribution from dn/dT and dL/dT in LNOI platform, whereas, there is a significant dominance of dL/dT in case of As_2S_3-LNOI platform. Similar behavior is also observed in Y45 orientation where dL/dT has more dominant contribution in As_2S_3-LNOI

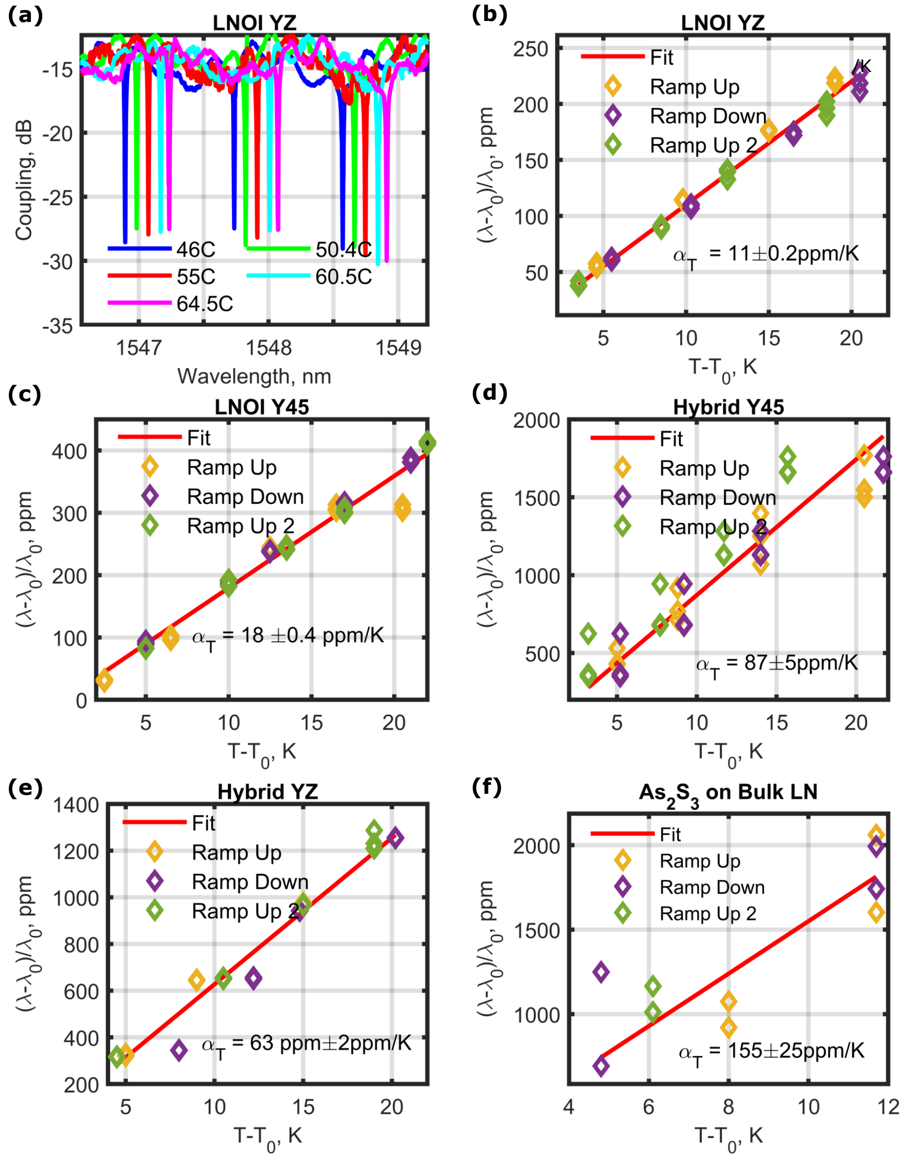

FIGURE 3.8: Measurement data for thermal coefficient extraction. (a) Transmission spectrum for a RT on LNOI in YZ orientation. Extraction of α_T, ppm/K for optical waveguide on (b) LNOI YZ, (c) LNOI Y45, (d) As_2S_3-LN Y45, (e) As_2S_3-LN YZ (f) (d) As_2S_3 on bulk LN.

platform. These experimental extractions reveal that thermal expansion of As_2S_3 would dominate over thermo-optic contribution for a hybrid material platform.

CHAPTER 4

Acoustic Devices

Two material stacks for acousto-optic applications are studied. First, As_2S_3 on oxide on bulk LN for low (~MHz) frequency application, and the second is As_2S_3 on LNOI for high frequency (~GHz) AO interaction. In both cases, acoustic waves are generated using interdigitated transducers (IDTs) [30]. Here acoustic structures that do not require release from the substrate are considered, in order to facilitate integration between acoustics and photonics. For low frequency (LF) acoustics, surface acoustic wave (SAW) is explored and for high frequency (HF) acoustics, considerations are resorted to the shear horizontal (SH_0) vibrations. The LF device is an acoustic resonator structure with reflectors, which attains high mechanical quality factor (Q), whereas, the HF device launches propagating SH_0 acoustic wave using IDTs. In case of HF acoustics, they do not exhibit a Q enhancement like the LF acoustic cavity case, but they permit to study the impact of acoustic waves on optical modulation without resorting to fabricating a multitude of fixed structures having different relative spatial separations between the acoustic resonator and the optical waveguide. For HF demonstration, IDT only structure is a design choice which simplifies the integration of photonics with acoustics as compared to the case of acoustic resonator, where nodes for placing photonic components become fixed and a high precision is required for integration success.

4.1 Low Frequency Acoustics

4.1.1 Motivation

The SAW cavity operating at low frequency was developed for a specific inertial sensing application: the acousto-optic gyroscope (AOG) project, of which this effort was a part [6]. The SAW device operates at an acoustic wavelength (Λ) of 30 μm. This was selected to meet the project requirement which served the following purposes:

- Utilization of a robust SAW cavity design which provides significant AO modulation enhancement due the acoustic Q-factor
- Large acoustic wavelength (Λ) allows large alignment tolerance for the acoustic and the photonic device interaction
- Large Λ also enables stronger AO overlap as the dimension of the optical waveguide is a small fraction of it
- Acoustic medium LN and photonic medium As_2S_3 could be separated by an oxide cladding layer and still induce strain in the photonic medium to achieve AO modulation

4.1.2 Design Consideration

For any SAW technology, the design challenge stems from the generation and control of the wave itself which can only be successfully done with the understanding of the piezoelectric substrate and its proper evaluation. The key parameters of interest are the surface velocity and electromechanical coupling coefficient (K_t^2). The K_t^2 determines how much electrical energy is coupled mechanically to the substrate, which is required to be as high as possible for efficient coupling and it's calculation method can be found in [31]. Whereas, the velocity is important to have values that ensures lowest relative velocity difference for the drive and the sense resonator (located orthogonal to each other) for the aforementioned application.

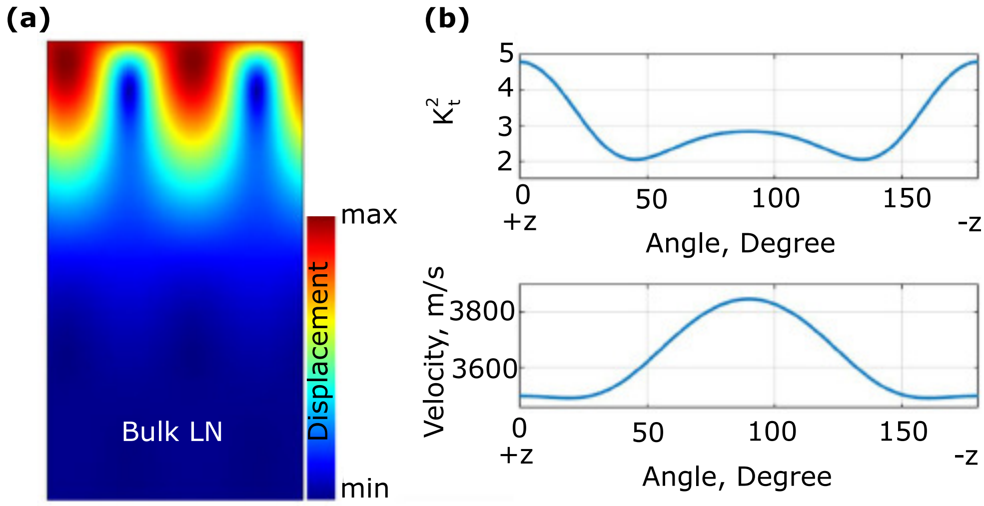

FIGURE 4.1: Material properties for Y-xut bulk LN: (a) total displacement due to SAW wave propagation from 2D Eigen mode simulation in COMSOL. (b) K_t^2 and velocity for SAW wave propagation.

There are various piezoelectric substrates and materials studied in literature [32] where the highest reported K_t^2 for Rayleigh SAW was found to be in LN. For this reason, it was selected as the material for the implementation of the gyroscope. K_t^2 and surface velocity were extracted from COMSOL eigenfrequency simulations using piezoelectric multiphysics, which couples structural mechanics and electrostatic physics. Fig. 4.1(a) shows an eigen unit of one Λ with Flouqet boundary condition on both sides. By defining constant amplitude across the aperture, the wave was simulated in 2D in COMSOL. K_t^2 and surface velocity for SAWs propagating in different directions for a Y-cut LN is shown in fig. 4.1(b). This particular cut of LN offers orthogonal crystal symmetry where the dimensions of the acoustic wavelength could be kept the same to achieve the frequency matching in orthogonal directions.

A detailed analysis of the design consideration and procedure can be found in [33].

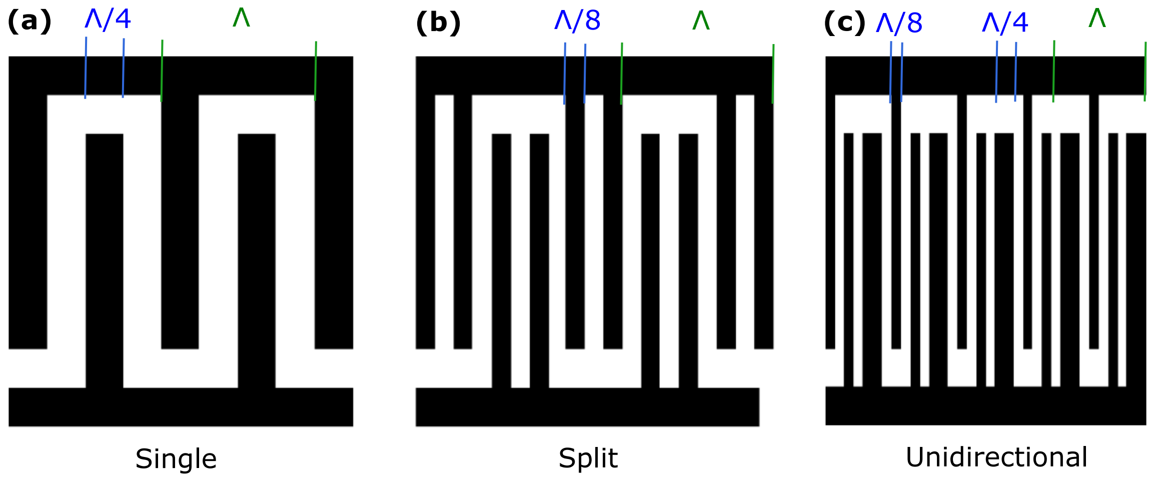

Figure 4.2: Different types of IDT structure: (a) single tap, (b) split and (c) single phase unidirectional.

IDTs [30] consist of a sequence of vertical metallic electrodes (or fingers) connected to two parallel bus bars. An alternating voltage signal applied to these IDTs, results in the expansion and contraction of the piezoelectric material underneath, generating a mechanical wave. This reciprocal device can also convert a mechanical wave in a piezoelectric substrate to a voltage. IDTs can be used to excite different modes and harmonics [34]. We focused on the 1^{st} order mode of Rayleigh SAWs for this particular device. Schematic structure for different kinds of IDTs can be found in fig. 4.2. From the figure shown, the disadvantage of split IDT and single phase unidirectional IDT (SPUDT) is that they required higher resolution lithography process compared to single tap IDT. We have picked single tap electrode IDTs for SAW generation.

4.1.3 LF Acoustic Resonator

As we have already mentioned, the LF SAW device is designed to operate at an acoustic wavelength (Λ) of 30 μm and for launching the SAW wave, single electrode type IDT is used, which is popular for its structural simplicity and relatively wide finger width ($\Lambda/4$ = 7.5 μm) relaxing the required photolithographic resolution [35].

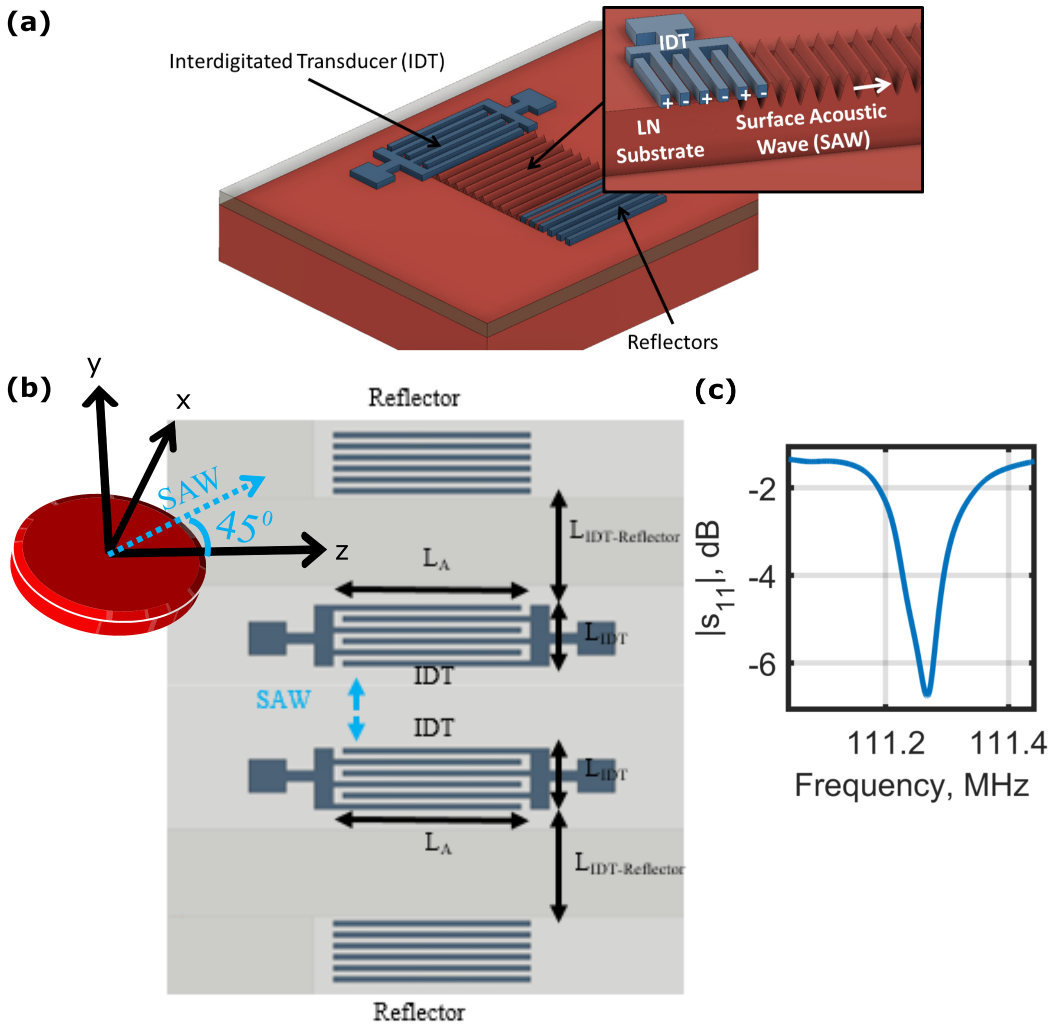

Figure 4.3: Low frequency SAW device: (a) schematic of the SAW cavity, (b) different parameters for SAW cavity design and (c) s_{11} frequency response for the one-port acoustic device.

As can be seen in fig. 4.3(a) and (b), the SAW generated on a Y-cut LN substrate propagating in Y45 direction (45^0 deviated from z direction). To ensure a standing wave pattern, mechanical reflection is achieved by an equivalent reflector grating structure with a periodicity of $\Lambda/2$ = 15 μm and a number of fingers equal to 400. This number of reflector fingers is sufficiently large to ensure that the SAW resonator attains a high quality factor (Q). The acoustic device has an aperture length (L_Λ) of 2400 μm to harness strong AO interactions. The number of IDT fingers is chosen to be 28 in order to match the motional resistance of the SAW resonator [17] to conventional radio frequency source impedance (50 Ω).

After building the IDT device, it was driven by a vector network analyzer (VNA) to determine its frequency response. Using a single port measurement, the SAW resonator's reflection coefficient (s_{11}) was measured to extract its Q (fig. 4.3(c)), which was found to be ~1200. In this implementation, the device Q is likely limited by the propagation loss resulting from diffraction, beam steering and in part by limited reflections from the acoustic gratings [18]. Effective SAW power put to the cavity, P_e, is computed as a function of the input electric power (P_{in}) as: $P_e = (1-|s_{11}|^2)P_{in}$. Fig. 4.3(c) shows the $|s_{11}|$ spectrum where the cavity achieved resonant boundary conditions at 111.27 MHz. The RF signal induces only SAW mode, which create a standing SAW inside the acoustic cavity.

4.2 High Frequency Acoustics

Phonons at gigahertz frequencies interact with electrons, photons, and atomic systems in solids, and therefore, have extensive applications in nonreciprocal light transmission [36, 37, 38, 39, 40, 41], modulation [7], frequency shifting [42], and signal processing [43, 44, 45]. Our approach to demonstrate a high acoustic frequency (~GHz) platform can be a key component for these applications as well as in stimulated Brillouin scattering (SBS) [46] and beam steering [47].

4.2.1 Design Considerations

To build a HF AOM platform, first thing that we need is to develop an acoustic device which can generate such acoustic signal on the LNOI platform. In case of LF AOM, it is possible to decouple the acoustic device on LN and photonic device on As_2S_3 using an oxide layer in between these materials. The key of success for such design is a large Λ which ensured acoustic energy confinement into the thin film As_2S_3 (for Rayleigh SAW most acoustic energy is confined within the 10% of Λ [48]). However, in high frequency AOM, As_2S_3 has to be directly deposited on LNOI because of the small Λ (~ 3.4 μm to achieve 1 GHz acoustic frequency) which limits the extent of acoustic energy confinement. We have explored both Y-cut and X-cut LNOI to integrate As_2S_3 on them and to determine their material properties and prospect for AOM applications. As a starting point we targeted at least 1 GHz as the operating frequency. Indeed higher frequency designs may be possible, but that comes at the expense of many fabrication challenges and precision requirements. Whereas, choice of 1 GHz touches the high frequency (~GHz) operation range with relatively relaxed minimum feature requirements for the acoustic and photonic devices as well as easier the fabrication process and precision requirements. The intent of this research endeavor is to qualify As_2S_3 as an enabling material which helps improve the optical phase modulation efficiency of the LNOI material platform in orientations which offers poor efficiency, as limited by the anisotropy of the piezoelectric material.

For successful generation of acoustic waves on LNOI, it's piezoelectric properties has to be investigated first. Therefore, we study the K_t^2 for both SAW mode and shear horizontal (SH_0) acoustic modes in Y-cut and X-cut LNOI as in Fig. 4.4. In a SH_0 wave, the displacement is parallel to the substrate's

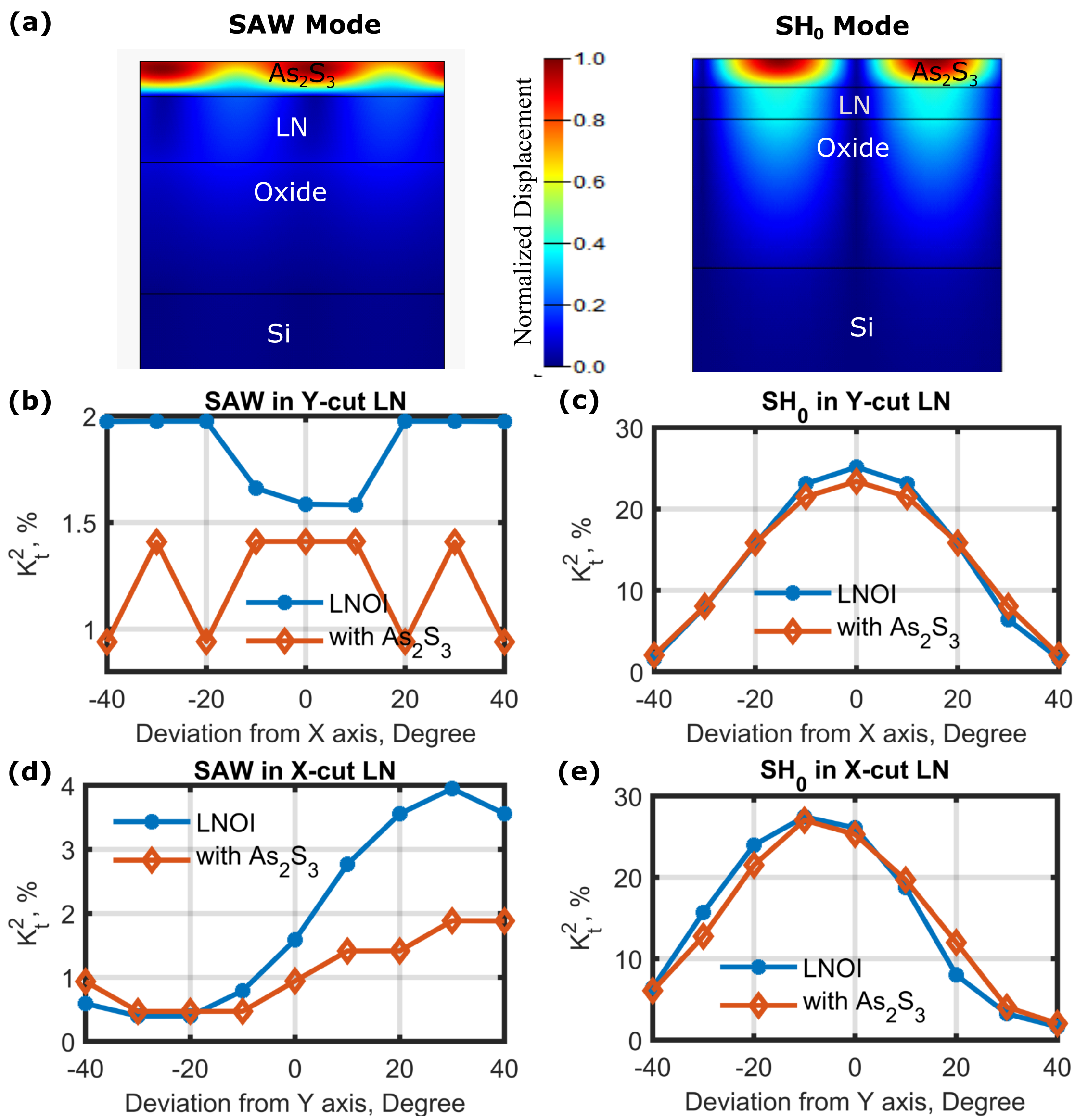

Figure 4.4: (a) COMSOL 2D unit cell model showing the SAW displacement mode on LNOI and SH_0 displacement mode on guided SH_0 structure with oxide as under layer and Si as substrate. The faces of each structure except for top and bottom surfaces have periodic Floquet boundary conditions. Such conditions ensure treating the unit cell as forming an infinite long plate. The colors in images represent the intensity of the total displacement and are normalized. They are used to represent the mode of vibration. Dependence of K_t^2 on crystal orientation on Y-cut LNOI for (b) SAW and (c) SH_0 and on X-cut LNOI for (d) SAW and (e) SH_0.

surface and perpendicular to the propagation direction. The SH wave has a slight advantage over Rayleigh SAWs as the former possess slightly higher phase velocity offering high frequency for the same acoustic wavelength. Fig. 4.4(a) shows displacement mode for both SAW and SH_0 with As_2S_3 on top of LNOI structure. The K_t^2 study includes both LNOI and As_2S_3-LN hybrid structure. When As_2S_3 is added on LNOI K_t^2 is significantly lowered (below 2%) for SAW mode on both cut of LNOI, as clearly shown in Fig. 4.4(b) and (d). On the contrary, the SH_0 demonstrates significantly higher K_t^2 for both cuts of LNOI, even after the addition of As_2S_3 on them as in Fig. 4.4(c) and (e). The LNOI which is used in this study had a LN film thickness of 300nm, oxide thickness of 1.4μm and As_2S_3 thickness of 270nm. The LNOI layer stack choice is determined by the X-cut LNOI wafer available in our inventory, using which we could verify our study experimentally.

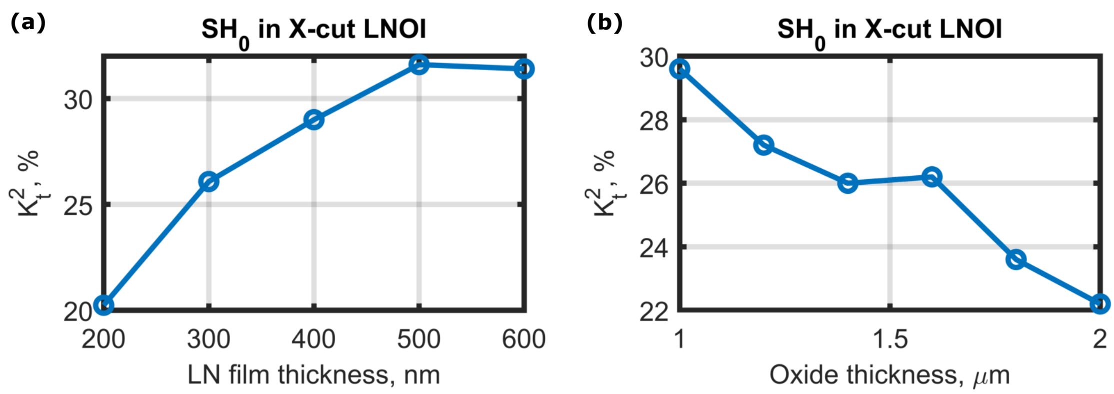

Figure 4.5: Dependence of K_t^2 on (a) LN film thickness and (b) bottom oxide thickness.

Both acoustic and photonic device performance are affected by LN film thickness and the oxide thickness. Fig. 4.5(a) shows K_t^2 dependence on LN film thickness for a oxide thickness of 1.4 μm and Fig. 4.5(b) shows dependence on oxide thickness for a LN film thickness of 300 nm. The X-cut LNOI available in our inventory has the following specification: LN film thickness 300 nm, oxide thickness 1.4 μm and Si as substrate.

4.2.2 Device Design and Experimental Results

From here on, our analysis only involve SH_0, not SAW mode. For AO modulation involving As_2S_3, strain components S_1 and S_2 are of utmost importance (see section 5.1.3 for details). COMSOL simulation of SAW and SH_0 mode reveals that amplitudes of these two strain components close to the As_2S_3 surface, are of the same order of magnitude for both the acoustic modes. It would also be interesting to study SAW mode for As_2S_3 on LNOI platform, however, we choose not to pursue it because of the very low K_t^2 for SAW mode. A very low K_t^2 means impedance of the electrode is likely to grow, requiring a larger acoustic device footprint for impedance matching. A larger device footprint would reduce our ability to vary experimental parameters on the limited number of substrates available. For experimental demonstration, we choose SH_0 mode for high frequency AO platform because of the high K_t^2 achievable on X-cut LNOI even after As_2S_3 deposition on it.

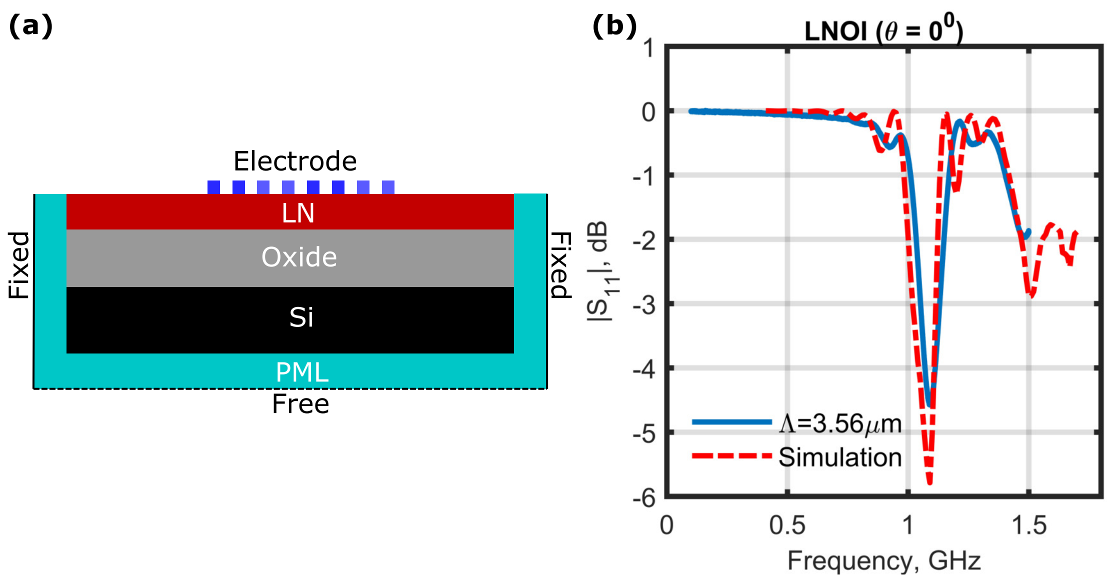

FIGURE 4.6: Propagating wave generation using split IDTs: (a) schematic simulation setup and boundary conditions, (b) frequency response comparison between simulation and experiment.

According to the unit cell simulation and literature [49], expected surface velocity for SH_0 is ~3800 m/sec. Therefore, we choose Λ between 3.24 μm and 3.56 μm to ensure an acoustic frequency of operation above 1 GHz. Fig. 4.6(a) shows a 2D simulation setup for studying the behavior of the split IDT structure launching propagating SH_0 on X-cut LNOI. Single type IDTs are narrowband compared to split type IDTs. Because of its narrowband single IDTs behaves more like resonator than an ideal IDT. As we are planning on using IDTs to create travelling wave only to study the frequency response, split IDTs are a better choice in terms of broadband operation. Even though the minimum feature size we need to reach with split IDT is around ~425 nm, this is achievable with e-beam lithography. A 2D COMSOL simulation of split IDT setup is formed by a metal grating structure on As_2S_3 on LNOI stack to study its frequency response. The IDTs are bidirectional (also called as double electrode IDTs with $\Lambda/8$ as line and spacing geometrical widths) and they were used to avoid internal reflections during excitation. A perfectly matched layer is applied on both sides of the IDTs and the bottom of Si layer (highlighted as PML). The thickness of Si is set to 10Λ (sufficiently large to ensure it behaves as a thick substrate without dramatically increasing required mesh number and simulation time). A frequency domain simulation was run with physics components such as solid mechanics and electrostatics including piezoelectric effect.

For the metal electrode of the IDTs we chose aluminum (Al) over tungsten (W) or platinum (Pt). Being a lighter metal its effects are less pronounced on the piezoelectric substrate, therefore, we can expect to have higher acoustic frequency with this metal. Besides, we have had vast process experience with e-beam resist for Al. Utilization of such process eased fabrication time and

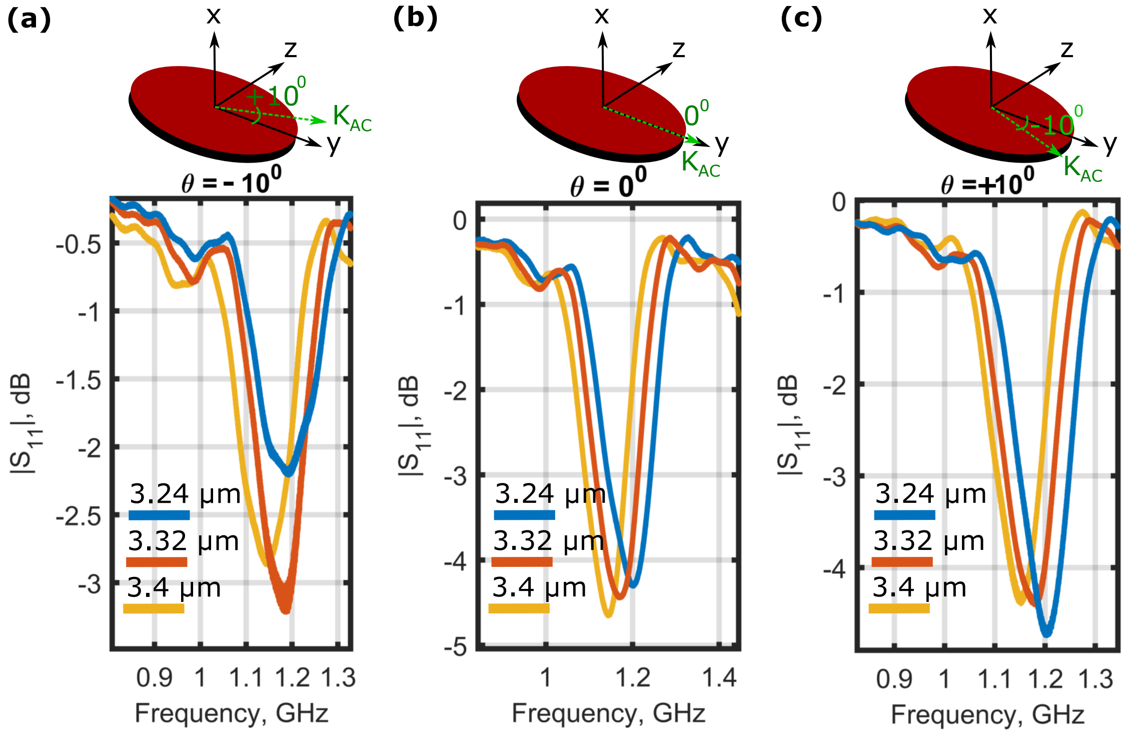

Figure 4.7: $|S_{11}|$ measurement for SH_0 with various acoustic wavelength propagating on a X-cut LNOI in directions deviated from the y-axis by the angle of (a) -10^0, (b) 0^0 and (c) +10^0.

difficulties. Thickness of Al was chosen to be 150 nm which was determined by the fabrication process to achieve a high yield. Fig. 4.6(b) shows frequency response (reflection parameter $|S_{11}|$, measured by vector network analyzer) comparison between simulation and experimental measurement which are in good agreement with each other. A traveling SH_0 wave is being launched at a frequency of 1.09 GHz. Here, SH_0 is propagating in y-direction on a X-cut LNOI where θ=0^0 represents the propagation direction from y-axis. Surface velocity of the acoustic wave is 3880 m/s which is a little slower than the value of 4200 m/s mentioned in literature [49].We chose 18 as the number of IDT finger pairs in order to match the RF source impedance (50 Ω). Measurements shows the IDT impedance at 1.09 GHz is 200 Ω, a large mismatch with the source impedance which is reducing the power conversion

Parameter	Device 1	Device 2	Device 3
Acoustic wavelength, μm	3.24	3.32	3.4
Aperture length, μm	150		
Finger width, nm	405	415	425
Number of finger pairs	18		
Frequency, GHz	1.203 (θ=-10^0) 1.201 (θ=0^0) 1.19 (θ=+10^0)	1.18 (θ=-10^0) 1.172 (θ=0^0) 1.187 (θ=+10^0)	1.152 (θ=-10^0) 1.144 (θ=0^0) 1.147 (θ=+10^0)
EM Coupling, K$_t^2$ %	24.4 (θ=-10^0) 21.3 (θ=0^0) 19.5 (θ=+10^0)	19.7 (θ=-10^0) 20.6 (θ=0^0) 19.8 (θ=+10^0)	21 (θ=-10^0) 19.7 (θ=0^0) 19.8 (θ=+10^0)
Static capacitance, pF	0.4 (θ=-10^0) 0.51 (θ=0^0) 0.49 (θ=-10^0)	0.5 (θ=-10^0) 0.53 (θ=0^0) 0.49 (θ=+10^0)	0.47 (θ=-10^0) 0.52 (θ=0^0) 0.48 (θ=+10^0)
Impedance, Ω	333 (θ=-10^0) 203 (θ=0^0) 184 (θ=+10^0)	268 (θ=-10^0) 196 (θ=0^0) 199 (θ=+10^0)	300 (θ=-10^0) 188 (θ=0^0) 199 (θ=+10^0)

efficiency from electrical to acoustic power. Increasing the number of finger pairs can solve this problem of impedance mismatch. Measured static capacitance of the IDT device is 0.5 pF. Fig. 4.6(b) also shows another acoustic mode launching near 1.5 GHz, which is mostly leaking energy into the substrate.

Fig. 4.7 shows $|S_{11}|$ measurement for IDTs generating SH$_0$ wave with various acoustic wavelength, propagating in directions deviated from y-axis by different angles (θ = -10^0, 0^0 and +10^0). Measured values for K_t^2 in different directions are as follows: 21.4% for θ= -10^0, 19.7% for θ = 0^0 and 19.2% for θ = +10^0. Device geometry related and measured parameters for the devices presented in Fig. 4.7 are listed in Table 4.2.2. In the following chapter, an envisioned AOM device is presented where these IDT devices could be used for demonstrating HF AOM.

Chapter 5

Integration of Acoustic and Photonic Device

In this chapter we discuss integration of the acoustic and photonic devices. Firstly, we discuss such integration for LF AOM, which is used to extract AO properties of thin film As_2S_3 and to demonstrate AOM functionality in As_2S_3 on oxide on LN platform decoupling the acoutic from the photonic device. Later, we discuss As_2S_3 on LNOI as a prospective material platform for HF AOM application, where we compare LNOI to hybrid As_2S_3-LN thin film platform.

5.1 Low Frequency Acousto-optic Modulator

We have demonstrated an AOM formed by an Arsenic Trisulfide (As_2S_3) Mach-Zehnder interferometer (MZI), operating in a push-pull configuration and placed inside a surface acoustic wave (SAW) cavity on a Y-cut Lithium Niobate (LN). This is the first demonstration of such an AOM in this As_2S_3 on oxide on LN platform. In this approach, the high index contrast of As_2S_3 waveguides is exploited to attain a high optical confinement. Additionally, the placement of the photonic MZI inside the SAW cavity enhances the AO interaction due to the high quality factor (Q) of the SAW resonator. An analytical expression that describes such enhancement as a function of the AO coefficient of As_2S_3 is derived in conjunction with COMSOL finite element methods to describe strain in the SAW cavity. By fitting this expression to experimental data, the AO coefficient (p_{11} and p_{12}, where $p_{11} \approx p_{12}$) for As_2S_3 is extracted at the wavelength of 1550 nm. This is the first time that the AO coefficient of thin film As_2S_3 is experimentally derived.

5.1.1 Motivation

In this modulator demonstration, we have exploited the piezoelectric properties of the LN substrate to generate SAWs and used As_2S_3 waveguides to form the arms of a MZI to achieve strain induced optical phase modulation. Amorphous As_2S_3 has higher AO coefficients than that of LN or GaAs [50], hence it is a very promising material for the making of small scale and on-chip AOMs. Although AO properties of As_2S_3 have been used to demonstrate on-chip Brillouin scattering devices [21, 14], to our knowledge, no AOMs have been built using a hybrid LN and As_2S_3 platform. Most importantly, the AO coefficients of As_2S_3 have never been experimentally extracted in thin films. The integration of electro-acoustic transducers in LN with As_2S_3 enables new opportunity in the development of compact AOMs. Through the demonstration of this modulator:

- We devise an analytical model of the MZI-AOM, validate it through finite element methods, and use it to extract, for the first time, the AO coefficient of thin film As_2S_3 at an optical wavelength of 1550 nm
- Discover the effect of dominant strain components on the modulation strength
- Use it as a proof of the concept that As_2S_3 for AOM could lead to more efficient designs not only because of the large AO coefficients, but also because of the isotropic nature of the film, which facilitates

decoupling of the design of photonic and acoustic components (different from LN or GaAs in which the anisotropic nature of the crystal inevitably couples the two domains)

5.1.2 Integrated Acoustic and Photonic Device

The LF AO modulator device consists of a symmetric SAW cavity with two interdigitated transducers (IDTs) and two reflectors accommodating MZI arms in between IDTs and reflector pairs (as in fig. 5.1(a) and (b)). Here IDTs and reflectors are placed on top of the LN substrate, whereas, the MZI and other photonic components are patterned in an As_2S_3 layer, which is deposited over an oxide cladding layer (fig. 5.1(c)). The oxide cladding layer enables efficient injection of light using grating couplers and strong optical mode confinement inside the As_2S_3 waveguide core [19] at the cost of a weaker strain field in the As_2S_3 itself. When an electrical signal is applied to the IDTs, an acoustic wave is induced inside the SAW cavity resulting in a standing wave pattern. By careful positioning of two MZI arms, the strain induced on the two arms can be maximized to harness strong AO modulation. The SAW device is designed to operate at an acoustic wavelength (Λ) of 30 μm as already discussed in section 4.1.3, but the concepts presented herein can be extended to other wavelengths. For launching the SAW wave, single tap IDT is used, which is popular for its structural simplicity and relatively wide strip width ($\Lambda/4$ = 7.5 μm) relaxing the required lithographic resolution [35].

To ensure a standing wave pattern, mechanical reflection is achieved by an equivalent reflector grating structure. Light is injected into the As_2S_3 strip waveguides with a dimension of 1.7 × 0.33 μm (dimensions are optimized for efficient light injection and lower propagation loss) from an external laser

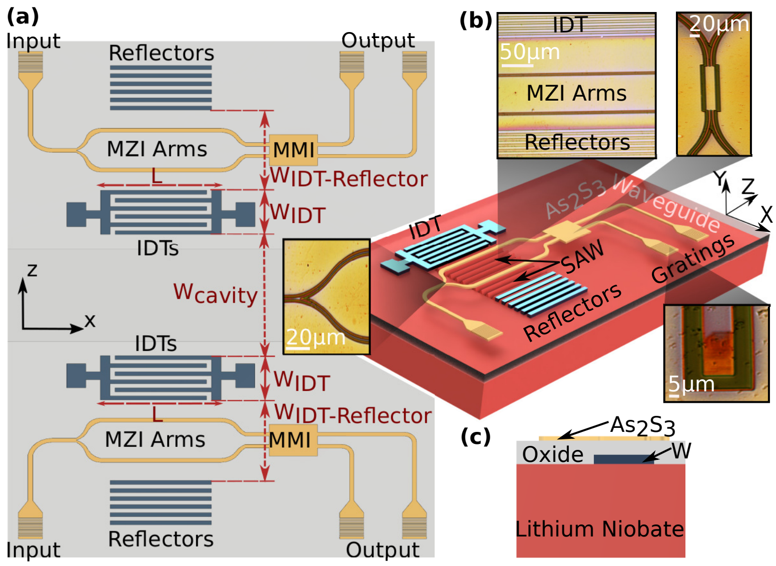

FIGURE 5.1: Rendering of device for AOM measurement with As_2S_3 MZI on Lithium Niobate platform. (a) Top view of the device, (b) schematic of the device with a set of IDT and reflector (inset: optical microscope images of the tested device), and (c) cross section showing the film stack. As_2S_3 photonic components are displayed as discrete structures (i.e. waveguides) in the schematic whereas in the experimental device, As_2S_3 film covers the entire sample surface. 3 μm wide trenches are etched in As_2S_3 on either side of the wire waveguide as shown in the optical microscope image.

source through a grating coupler. The input optical signal is then split into two identical MZI arms using a Y-junction splitter. The phase of the light traveling through the two As_2S_3 arms of the MZI gets modulated due to the strain induced refractive index modulation. The two arms are separated by an odd multiple of $\Lambda/2$ to ensure push-pull operation. The modulated signal of the two arms then combines through a 2x2 multi-mode interference (MMI) coupler (with a dimension of $86 \times 12 \times 0.33$ μm) which translates the phase modulation to amplitude modulation and splits the input power equally into two output ports.

5.1.3 Principle of Operation

The refractive index modulation induced in the MZI arms by the AO effect is described by the following expression:

$$\Delta n_i = -\frac{1}{2} n_i^3 p_{ij} S_j (i, j = 1, 2, .., 6) \tag{5.1}$$

with p_{ij} is the ij-th AO coefficient of the material and S_j is representing the j-th component of the strain field tensor [51]. The repeated index in the subscript implies summation over that index. This device was built on a Y-cut LN wafer, and acoustic transducers were rotated by 45^0 about the crystal y'-axis with respect to the crystal x' axis.

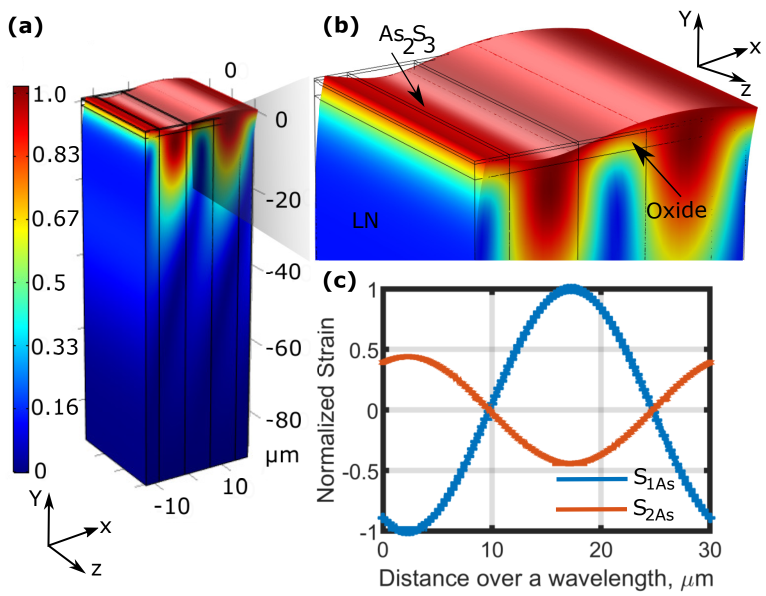

Figure 5.2: (a) Normalized displacement due to the SAW propagation obtained from 3D COMSOL simulation and (b) enlarged view of material stack. (c) Dominant normalized (to maximum amplitude) strain components at the oxide and As_2S_3 interface.

Fig. 5.2 shows the rotated crystal coordinate system, which is represented by (x,y,z). The (x',y',z') notation is used for the non-rotated Y-cut crystal. For a Rayleigh SAW wave, the strain field vector of the surface acoustic wave propagating along the x-axis on top of the LN surface can be expressed as: $(S_{1LN}\ S_{2LN}\ S_{3LN}\ S_{4LN}\ S_{5LN}\ S_{6LN})$[1], where S_1 is the strain field along x-direction and S_2 is the strain field in y-direction. The amplitude of the other strain components is negligible or acting along the aperture, L, of the SAW resonator (fig. 5.2(a), hence ineffective in modulating light. Our direction of interest is transverse to the direction of the aperture length. 3D Finite Element Method (FEM) using COMSOL software was used to estimate the relative amplitudes of these two main strain components for the SAW propagating in the film stack along the x-axis.

Figure 5.2(a) shows the schematic of a SAW wave propagation and the deformations in the material layer stack obtained from COMSOL simulation. An enlarged view of the deformations close to the material stack surface is shown in fig. 5.2(b) which identifies the different material layers in the simulation setup. Boundary conditions for both solid mechanics and electrostatics modules used in this 3D COMSOL simulation are as follows: Floquet periodicity for the two faces parallel to YZ plane, and continuity for the two faces parallel to XY plane. Additionally, in the solid mechanics module, fixed and free boundary conditions were used for the bottom XZ plane and the top face parallel to XZ plane, respectively. The distribution of the strain components at the interface of the As_2S_3 and the cladding oxide[2] layer are plotted versus the propagation direction (along x) in fig. 5.2(c), over a distance of one Λ. From this plot it is clear that at the oxide-As_2S_3 interface, S_{2As} is out of phase with S_{1As} with relative amplitudes, $|S_{2As}| = 0.44 \times |S_{1As}|$. Assuming S_{1As} to be the dominant strain component, the two arms of the MZI are placed at

[1] Strain field at LN and oxide interface is represented with $S_{\#LN}$

[2] Strain field at As_2S_3 and oxide interface is represented with $S_{\#As}$

a distance of $(n+\frac{1}{2})\Lambda$ (where $n = 1, 2, ..$) in order to maximize strain induced index modulation. It must be recalled that as shown in fig. 3.4(b), the optical waveguide in As_2S_3 is built by etching 3 μm wide trenches in a continuous As_2S_3 thin film to ensure strong optical mode confinement inside the wire waveguide. In our COMSOL test device, the As_2S_3 thin film is a continuous layer. Compared to the SAW wavelength (30 μm) these trenches are quite small. Furthermore, the cavity has a length of 125Λ and the majority of it is covered by a continuous film of As_2S_3. Given these considerations, the use of a continuous film in the COMSOL simulation of the SAW is a valid approximation. By placing the MZI arms at the maximum strain positions and considering the overlap between the optical field distribution $\Psi(x, y)$ inside the waveguide and the strain field $S(x, y)$, eqn. 5.1 can be modified assuming the perturbed waveguide solution [51, 52, 7] as:

$$
\begin{aligned}
\Delta n_x &= \frac{1}{2} n^3 p_{ij} \int\int S(x,y)|\Psi(x,y)|^2 dxdz \\
&= \frac{1}{2} n^3 (p_{11} S_{1As} + p_{12} S_{2As}) \Gamma_{AO}
\end{aligned}
\tag{5.2}
$$

where $\Gamma_{AO} = 0.97$, which is the AO overlap between the strain field and the optical mode inside the As_2S_3 [53], and assuming $p_{11} \approx p_{12}$ (as shown experimentally at 1150 nm [9]). Here, we have considered TE-like optical mode, meaning light is polarized in x-direction.

The energy density in the SAW cavity can be approximated by $U \approx \frac{1}{2}(S_{1As}C_{11As}S_{1As} + S_{1As}C_{12As}S_{2As} + S_{2As}C_{21As}S_{1As} + S_{2As}C_{22As}S_{2As})$ where S_{1As} and S_{2As} are the dominant strain components on the As_2S_3 thin film (from Fig. 5.2(c)). As U is integrated over the volume of the As_2S_3 thin film, we can calculate the total acoustic energy inside the As_2S_3 thin film and express it in terms of S_{1As} only as follows:

$$E_{As} = \frac{1}{4} \times 1.528 \times C_{As}|S_{1As}|^2 L_c L h_{As_2S_3} \tag{5.3}$$

Here $L_c = 2W_{IDT} + W_{cavity} + 2\Lambda/(r \times 4) + 2W_{IDT-Reflector}$, r is the reflectivity of acoustic grating [18] and $h_{As_2S_3}$ is the thickness of the As_2S_3 film [6]. While simplifying this equation, $S_{2As} \approx 0.44 S_{1As}$ was used. The shear modulus of As_2S_3 is assumed to be 40% of the elastic modulus (C_{As}) [28].

The total energy stored inside the SAW cavity (E) is related to the SAW Q factor as $E = P_e Q/\omega_m$ where P_e is the effective SAW power in the cavity, $\omega_m = 2\pi v_R/\Lambda$ is the angular resonance frequency, and $v_R = 3570$ m/s is the SAW velocity (from simulation). As per COMSOL 3D eigenfrequency simulation, only 1% of the total acoustic energy is confined inside the As_2S_3 thin film (power confinement inside the thin film may be enhanced by operating at higher acoustic frequencies). Therefore, the energy inside this thin film is $E_{As} = 0.01 \times QP_e/(2\pi v_R/\Lambda)$. Based on these considerations, the strain component in the x-direction in the As_2S_3 thin film can be deduced as:

$$|S_{1As}| = \sqrt{\frac{2 \times 0.01 \times Q\Lambda P_e}{1.528\pi C_{As} v_R L_c L h_{As_2S_3}}} \tag{5.4}$$

The phase change in one of the MZI arms can be written as the function of optical wavelength (λ), MZI arm length (= aperture length, L) and refractive index variation (Δn):

$$\theta_{AO} = \frac{2\pi}{\lambda} L \Delta n \tag{5.5}$$

Considering eqn. 5.1 and eqn. 5.4 and assuming push-pull operation of the MZI, the phase shift per unit square root of acoustic power (P_e) inside the SAW cavity, $\alpha_p = 2\theta_{AO}/\sqrt{P_e}$ can be derived as:

$$\alpha_p = \frac{2\pi}{\lambda} n^3 (p_{11} - 0.44 \times p_{12}) \Gamma_{AO} \sqrt{\frac{2 \times 0.01 \times Q \times \Lambda \times L}{1.528\pi C_{As} v_R L_c \times h_{As_2S_3}}} \tag{5.6}$$

The modulated light signal from two arms of the MZI combines into a 2×2 MMI coupler, which puts the two arms in quadrature and produces a signal proportional to the index modulation strength on each output waveguide. At the input port of the MMI coupler, the two arms of the MZI may introduce a phase difference due to fabrication imperfections denoted as $\Delta\theta_{MZI}$. Additionally, because of the MMI coupler a phase difference of θ_{MMI} is added between the two output arms of the MMI. Applying the Jacobi-Anger expansion to the output power expression (see detailed derivation in section 6.2), the fundamental modulated optical output power, H_1, and its two harmonics (H_2, H_3,) can be found to be equal to:

$$H_1 = -\frac{1}{2} P_{sub} J_1(\alpha_p \sqrt{P_e}) \sin\theta_0 \tag{5.7}$$

$$H_2 = -\frac{1}{2} P_{sub} J_2(\alpha_p \sqrt{P_e}) \cos\theta_0 \tag{5.8}$$

$$H_3 = \frac{1}{2} P_{sub} J_3(\alpha_p \sqrt{P_e}) \sin\theta_0 \tag{5.9}$$

where, $\theta_0 = \Delta\theta_{MZI} + \theta_{MMI}$ and P_{sub} represents the power amplitude of the modulated signal. By measuring the modulated optical output power and its two harmonics α_p and θ_0 can be extracted. Since α_p is a function of the EO coefficients in As_2S_3, using these analytical expressions and experimental data, the AO coefficients for As_2S_3 can be extracted.

5.1.4 Measurement Setup

The AOM measurement setup is shown in fig. 5.3. Light at 1550 nm from a Santec TSL-550 tunable laser source was fed into the device under test (DUT) through a vertical groove array holding a fiber and an on-chip grating coupler. The IDT was driven by an RF signal generator (E4433B ESG-D Series) at the center frequency of the SAW resonator which was determined to be, f_m = 111.27 MHz. Using a single port measurement, the SAW resonator's reflection coefficient (s_{11}) was measured to extract its Q, which was found to be ~1200. In this implementation, the device Q is likely limited by the propagation loss resulting from diffraction, beam steering and in part by limited reflections from the acoustic gratings [18]. Effective SAW power in the cavity, P_e, is computed as a function of the input electric power (P_{in}) as: $P_e = (1 - |s_{11}|^2)P_{in}$. The RF signal induces only SAW mode, which create a standing SAW inside the acoustic cavity. This standing SAW give rise to strain that deforms the MZI waveguide arms resulting in an optical phase modulated signals in the MZI arms operating in push-pull configuration. This means the refractive index of the MZI waveguides are varying sinusoidally at the frequency around f_m.

The MZI outputs were combined via a 2×2 MMI coupler which translates the optical phase modulation into the optical amplitude modulation. One of the MMI coupler outputs was coupled into the optical fiber through a grating coupler, which was connected to an Erbium-doped fiber amplifier (EDFA)

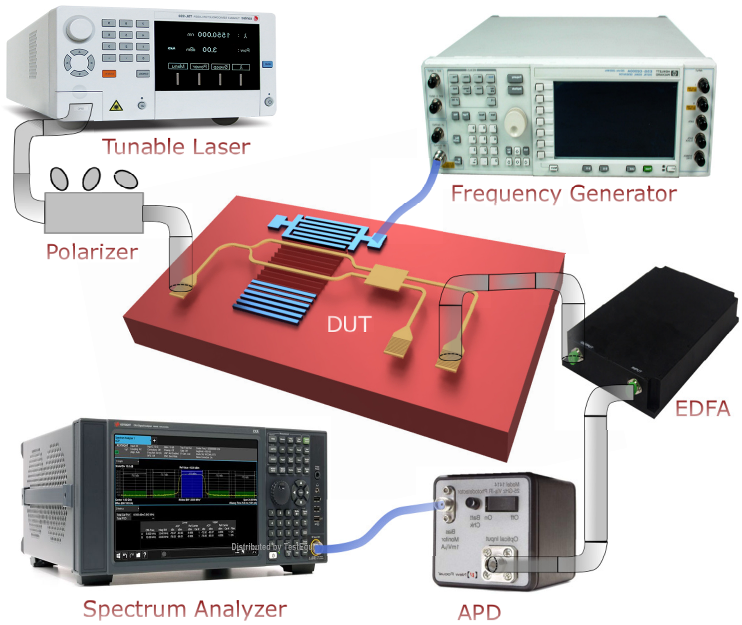

Figure 5.3: Experimental setup for AOM testing. Blue lines represent electrical connections, whereas, gray lines represent optical fiber connections.

to amplify the output signal and make sure it can be readily converted into an electrical signal through a high-speed avalanche photodiode (APD) with a sensitivity of 0.7 A/Watt which detects a sinusoidally varying photo-intensity signal. The coupling efficiency of each of the gratings was computed to be ~ -17 dB under the assumption that the MMI coupler loss is negligible and the As_2S_3 exhibits a propagation loss of ~4 dB/cm as previously extracted in[54]. Although the coupling efficiency of the uniform gratings used herein is low, the intensity of the fundamental and harmonic signals was sufficient to investigate the acousto-optic effect in As_2S_3. Adopting a non-uniform grating design and using a bottom mirror could dramatically improve the coupling losses as shown in [19]. In our device one of the output gratings was damaged during the fabrication process, therefore, we only measured the output from one of the two output ports. The output electrical signal was monitored through a Keysight N9000B CXA Spectrum Analyzer. We recorded the maximum output electrical power due optical modulation at frequency f_m from the spectrum analyzer, while varying the amount of P_e by tuning the alternating input acoustic power from the frequency generator.

5.1.5 Result Analysis

Our objective is to accurately extract the values of the elasto-optic coefficient independently of the various components' loss and phase mismatch between the MZI and MMI branches introduced by fabrication errors. To this extent, we have extracted the output optical power (H_1, H_2 and H_3) from the measured electrical power generated by the AOM at the fundamental frequency (P_1) and harmonics (P_2 and P_3) where $P \propto H^2$. By measuring the fundamental power and its harmonic, it is possible to extract the value of α_p independently of the system loss. For the DUT, parameters used for extracting α_p are listed in Table. 5.1. Similarly, phase difference due to fabrication imperfection and MMI coupler (θ_0) can also be extracted by taking the ratios between (H_1, H_2) and (H_3, H_2).

The modulus of the ratio of the modulated output optical power for the fundamental frequency and its harmonic component (H_1/H_3) equals to the ratio of the Bessel functions from eqn. 5.7 and eqn. 5.9. Since these Bessel functions are dependent on the acoustic power and α_p, their ratio could be fit to the experimental data obtained for H_1/H_3, solving for the value of α_p. Fig. 5.4(a) shows the fitting of the ratios to the experimental data and the value extracted for α_p is equal to 8.36 $rad/\sqrt{Watt}$. This value is larger than the state of the art AOMs in other AO materials such as GaAs [55] or LN [53]. Using eqn. 5.6 it is possible to extract the EO coefficients of As_sS_3 (where

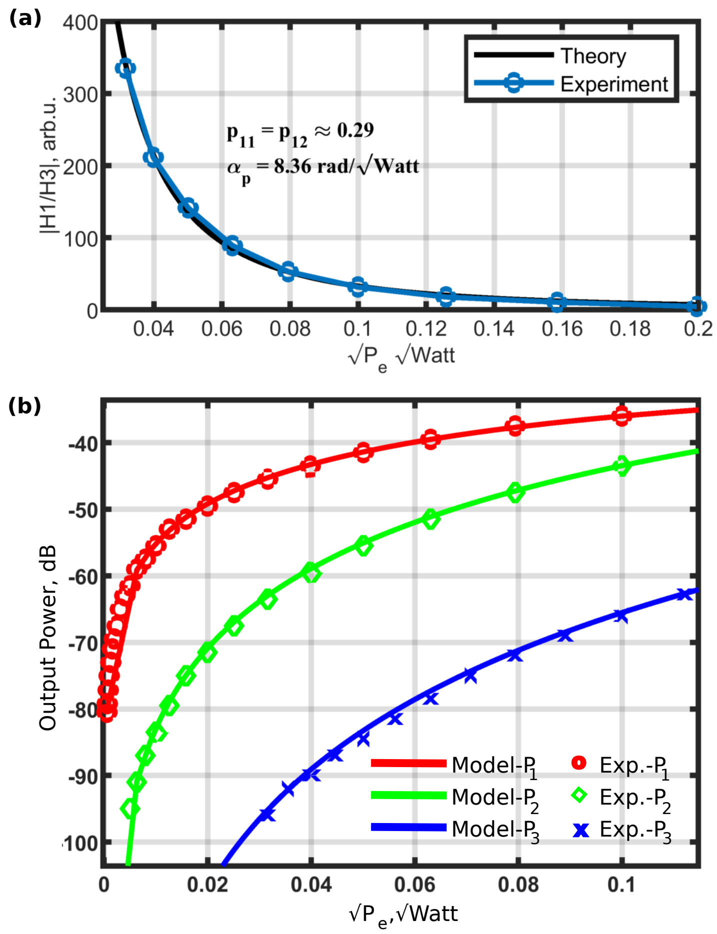

Figure 5.4: (a) Modulus of H_1/H_3 and extraction of $p_{11}(\approx p_{12})$. (b) Analytical expression fit to measured modulated output electrical power P_j (where j=1,2,3) which was converted from optical power recorded by the APD.

$p_{11} \approx p_{12}$ at 1550 nm [9]). The values for p_{11} and p_{12} were calculated to be 0.29 which is close to the value (p_{11} = 0.308 and p_{12} = 0.299) measured for the bulk material [9] at a wavelength of 1150 nm. θ_0 was also extracted to be 28^0. Note that in order to maximize the output modulated power, this angle should be 90^0, which could be attained by properly redesigning the MMI couplers after taking into account fabrication imperfections. Using the values for α_p and θ_0, the optical power described in eqn. 5.7, 5.8 and 5.9 are converted to the corresponding electrical power P_1, P_2 and P_3 and plotted

TABLE 5.1: Parameter set for EO coefficient extraction

Parameter	Symbol	Value	Unit
Optical wavelength	λ	1550	nm
Effective index	n	1.91	
As_2S_3 thickness	h	330	nm
Acousto-optic overlap	Γ_{AO}	0.97	
Acoustic wavelength	Λ	30	μm
Average SAW velocity	v_R	3570	ms^{-1}
Acoustic Q factor	Q	1200	
Aperture length	L	2400	μm
Effective SAW cavity length	L_c	5200	μm
As_2S_3 elastic modulus	C_{As}	16.6	GPa

along with the experimental measurement in fig. 5.4(b) to verify the validity of our extractions.

5.1.6 Acousto-Optic Figure of Merit

A large AO figure of merit (AOFOM) is desired for device applications. A number of AOFOMs has been defined and used for interpreting the usefulness of an AO material system. We have chosen M_2 as the AOFOM in our case which is defined as follows:

$$M_2 = \frac{n^6 p_{eff}^2}{\rho v_s^3} \tag{5.10}$$

where n is the index of refraction (effective index for the optical waveguide), p_{eff} is the effective AO coefficient of the AO interaction medium, ρ is the density of the medium and v_s is the surface acoustic velocity. M_2 is appropriate when AOFOM is defined to express the phase modulation efficiency or when the diffraction efficiency of an AO material system is the parameter of concern. However, it does not provide any insight into the modulation bandwidth or resolution. Our goal is to demonstrate that incorporating As_2S_3 with LN enhances the modulation efficiency of the material system compared to using LN or LNOI alone, as M_2 represents a factor in the phase modulation efficiency for the kind of AOM devices we are discussing here. The anisotropy of the LN medium makes some crystal orientations incapable of strong AO modulation which may be improved by making a hybrid material system with As_2S_3.

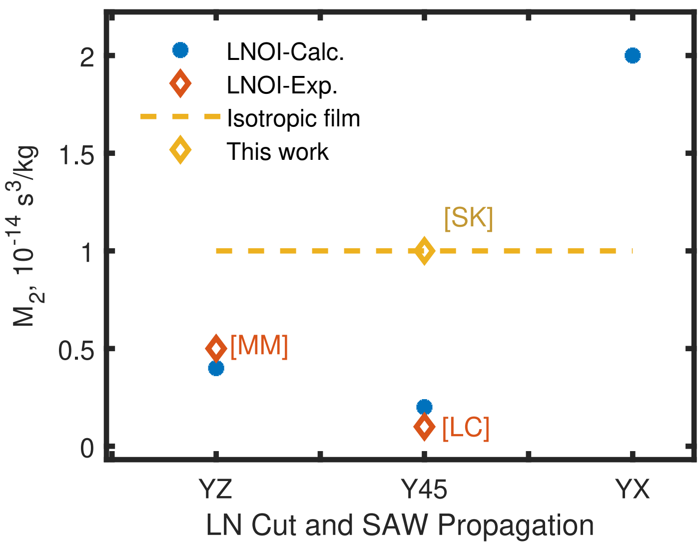

Figure 5.5: Acousto-optic figure of merit for AOMs on LNOI and As_2S_3 on oxide on LN. MM:[6] LC:[53] SK:[56]

Figure 5.5 shows M_2 calculated for AOMs in Y-cut LNOI for SAW propagation in z direction (YZ), in 45^0 deviated from z direction (Y45) and in x direction (YX). The calculation of p_{eff} is discussed in details in the following section 5.2. The calculated M_2 values are then compared to the experimental results for acoustic devices with same Λ and using MZI for AO interaction. The acoustic device in this bulk LN is similar to the ones on LNOI platform. We have integrated As_2S_3 with bulk LN as the photonic medium which demonstrates stronger value for M_2 experimentally. Such comparison shows that modulation efficiency can be significantly improved in Y-cut LN using As_2S_3 on oxide on LN platform, at least for SAW propagation between YZ and Y45 and light propagating orthogonal to the SAW propagation direction. Calculation shows that large M_2 value is achievable for SAW propagation in YX direction, however, that comes at the cost of low K_t^2 value.

5.2 High Frequency Acousto-optic Platform

The intrinsic material system property that determines the strength of AO interactions is the effective AO coefficient of the overall system. Effective index, acoustic wavelength (phase relationship between strain components and their amplitude) and acoustic mode velocity also plays vital role in modulation efficiency. For acousto-optic modulator (AOM) on LNOI system (SAW propagating in Y45 direction), p_{eff} has been determined to be 0.06 [53] and for As_2S_3 on oxide on LN it has been determined to be 0.14 [56] in low frequency (~MHz) application. To demonstrate a high performance AOM at high frequencies (~GHz), the material platform needs to support the acoustic and photonic properties listed in the table below.

Acoustic Properties	Photonic Properties
GHz frequency (wavelength ~ 3.4μm)	High effective index
Maximize effective AO coefficient	Maximize AO overlap in hybrid waveguide

To keep As_2S_3 thickness as low as possible, we prefer TE like mode operation in the As_2S_3 waveguide. For efficient light injection in As_2S_3-LN hybrid grating, optimal As_2S_3 thickness has been determined to be 270 nm. For TE like mode operation, cut-off width for As_2S_3-LN hybrid waveguide is ~800 nm. To maximize AO overlap, optical waveguide width has to be half of the acoustic wavelength. Keeping fabrication process bias in mind, we aim to reach the acoustic wavelength of 3.4 μm which corresponds to an acoustic frequency of 1.14 GHz. Besides high AO overlap, maximization of the effective AO coefficient is crucial. As discussed in [56], when the amplitude difference between S_{1As} and S_{2As} is maximum inside the As_2S_3 layer, the highest effective AO coefficient can be attained. The AOM that we have demonstrated in [56], cannot be scaled up to the acoustic frequency of our interest. In that case, the oxide thickness would be comparable to the acoustic wavelength and the acoustic energy in the As_2S_3 layer would be extremely small to induce any optical modulation.

5.2.1 Integration of As_2S_3 on LNOI

For an effective HF acousto optic platform, As_2S_3 is deposited directly on top of LNOI. In this kind of material stack, optical guided mode is shared between the thin film LN and As_2S_3. For an initial study, we wanted to split half of the optical energy into the LN and the other half into the As_2S_3 and understand how the addition of As_2S_3 affects the AO performance of LN. The effect of As_2S_3 thickness on the effective index of As_2S_3-LNOI hybrid waveguide is depicted in Fig. 5.6(a) where the waveguide thickness was fixed at 1.7 μm. The figure also shows the effect of waveguide width on the amount of power confinement inside the As_2S_3.

According to Eqn. 5.10 for stronger AO modulation, effective index needs to be large. To ensure strong acousto-optic overlap, the maximum allowed optical waveguide width is the half of the acoustic wavelength. For a high frequency modulator, the waveguide width is selected keeping in mind that inside the hybrid guiding medium, we want a 50-50 optical power split between As_2S_3 and LN during propagation. Higher index as well as lower width is achievable with higher As_2S_3 thickness. However, higher As_2S_3 thickness

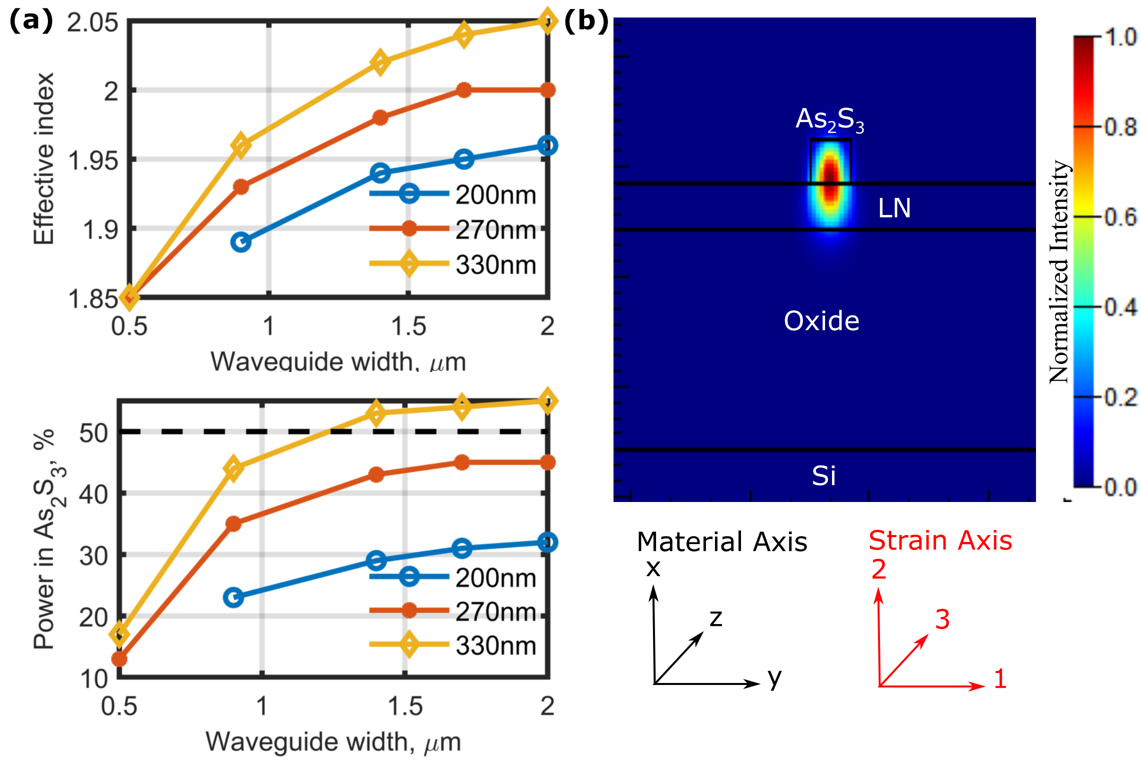

Figure 5.6: Waveguide analysis

means longer As_2S_3 deposition time as our available equipment can achieve a deposition rate of 60 nm/hour. Most importantly, thicker As_2S_3 means more arsenic contaminants are released during the etch process, which may surpass the maximum allowed quantity for As_2S_3 etch, a limit set by the lab safety protocol. Therefore, to reduce the amount of arsenic contaminants during the etch process, we settled for an As_2S_3 thickness of 270 nm which allows us to achieve both high effective index as well as almost equal power split between As_2S_3 and LN (45% and 55% respectively). Fig. 5.6(b) shows the normalized intensity distribution between the two guiding medium for As_2S_3 on X-cut LNOI for SH_0 propagating along y-axis. The figure also denotes the relevant material axial definition where x expresses the cut of the LNOI, y is the direction for acoustic wave propagation and z is the direction along the

IDT aperture. Corresponding equivalent strain axis where S_1 (strain component S_{11}) is acting along material y axis and S_2 (strain component S_{22}) is acting along material x axis. In the following sections, definitions like (x,y,z) would refer to the material axis and (1,2,3) would refer to the strain axis.

5.2.2 Calculation of Effective Acousto-optic Coefficient

To calculate the effective AO coefficient, it is important that the material axis and strain axis are related to each other in a consistent manner, to avoid confusion while determining the overlap integral between the optical and acoustic mode. Strain components are calculated using 2D COMSOL finite element simulation.

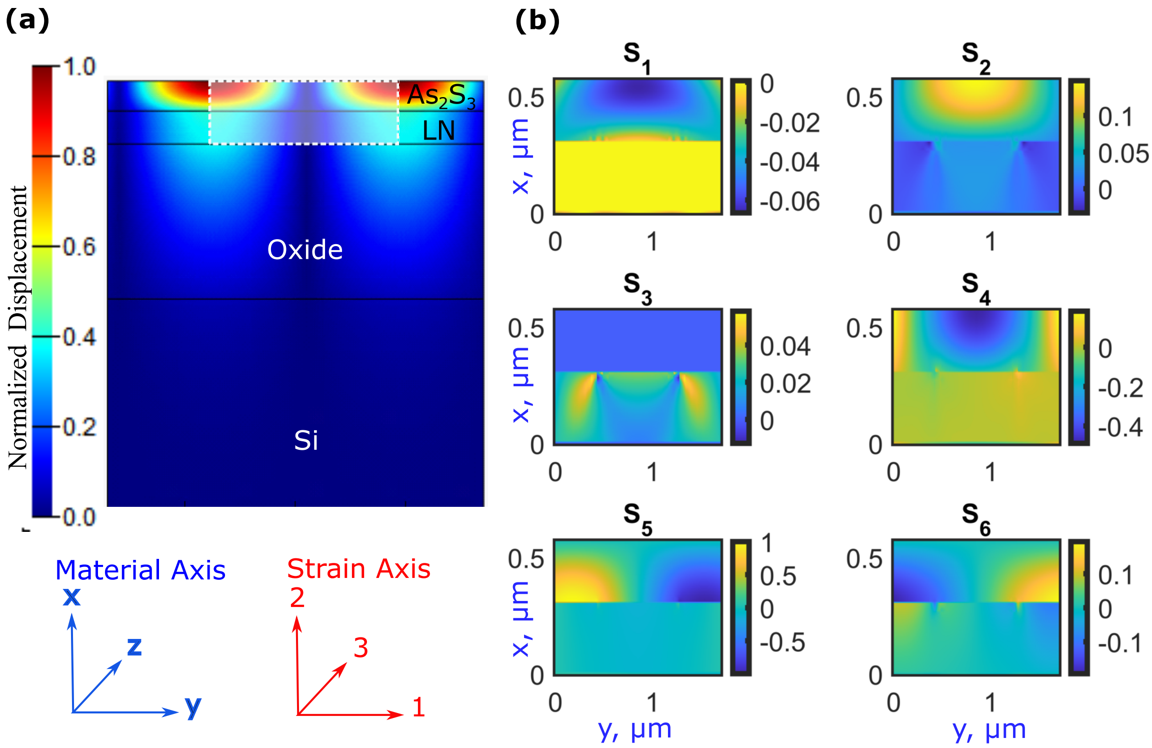

Figure 5.7: (a) Shear horizontal (SH_0) displacement mode. (b) Strain amplitude distribution within the 1.7 x 0.57 μm waveguide region.

Fig. 5.7(a) shows the total displacement for SH_0 mode for an unit cell. A white inset extending between As_2S_3 and LN layer shows an outline for the hybrid ridge waveguide of 1.7 μm width. This placement is chosen such a way that the strain components S_1 and S_2 has the maximum amplitude difference inside the As_2S_3 film, which is required for maximum p_{eff} as thoroughly discussed in section 5.1.3. Fig. 5.7(b) shows the strain distribution within the As_2S_3-LN hybrid waveguide structure. Strain amplitudes are normalized to the dominant shear strain component which is S_4 in this case. Before we could determine the performance of the hybrid AO platform for different orientation, we need to calculate the p_{eff} for the corresponding direction. First, we calculate p_{eff} for both As_2S_3 and LN independently. Because of its isotropic nature, As_2S_3 has only two AO coefficients p_{11} and p_{12} [9]. Effective AO coefficient for As_2S_3 can be defined as follows:

$$p^{As}_{peff,1} = p^{As}_{11}\Gamma^{As}_{AO,1} + p^{As}_{12}\Gamma^{As}_{AO,2} \tag{5.11}$$

Similarly effective AO coefficient for LN would be:

$$\begin{aligned} p^{LN}_{peff,i} &= p^{LN}_{i1}\Gamma^{LN}_{AO,1} + p^{LN}_{i2}\Gamma^{LN}_{AO,2} \\ &+ p^{LN}_{i3}\Gamma^{LN}_{AO,3} + p^{LN}_{i4}\Gamma^{LN}_{AO,4} \\ &+ p^{LN}_{i5}\Gamma^{LN}_{AO,5} + p^{LN}_{i6}\Gamma^{LN}_{AO,6} \end{aligned} \tag{5.12}$$

where i = 1 and

$$\Gamma^{(As/LN)}_{AO,j} = \frac{\iint_{(As/LN)} S_j(y,x)|E_i(y,x)|^2\,dy\,dx}{\iint_{(As/LN)} |E_i(y,x)|^2\,dy\,dx}$$

representing strain amplitude with $|S_j|$ which is normalized by the dominant strain component amplitude (S_4) because of the SH_0 propagation. Here, we assume fundamental TE like (polarized in y direction) optical mode confined inside the hybrid waveguide, half power of which is interacting with the strain components inside the As_2S_3 film and the other half power is interacting with the strain components inside the LN thin film. For $p^{LN}_{eff,i}$ the index i represents the polarization direction for light and j is indexed with 1 to 6 relating each strain components with electric field intensity to calculate the overlap integral. Γ represents the overlap integral between each strain component and the TE like optical mode where $|E_i(y,x)|^2$ represents normalized electric field intensity distribution for polarization direction related to i. Superscripts like As or LN represents the region inside As_2S_3 or LN respectively for the definition of p_{eff} or overlap integral Γ.

We have calculated p_{eff} for both As_2S_3 and LN independently, for different orientation of SH_0 propagation as well as parallel or perpendicular AO interaction. If the acoustic wave vector K_{AC} and optical wave vectors K_{OPT} are orthogonal to each other, such interaction is termed as perpendicular propagation. In cases where K_{AC} and K_{OPT} are co-directional, such interaction is termed as parallel propagation. For SH_0 propagating in y direction on a X-cut LNOI, effective AO coefficient for perpendicular setup would be labeled as $p^{LN}_{eff,1}$ to indicated light polarization along strain axis 1, and for parallel propagation it would be labeled as $p^{LN}_{eff,3}$ to indicate optical polarization in strain axis 3. Perpendicular setup is popularly used in modulator or sensing applications using MZI or resonators, whereas the parallel setup is used in optical diffraction or beam steering applications.

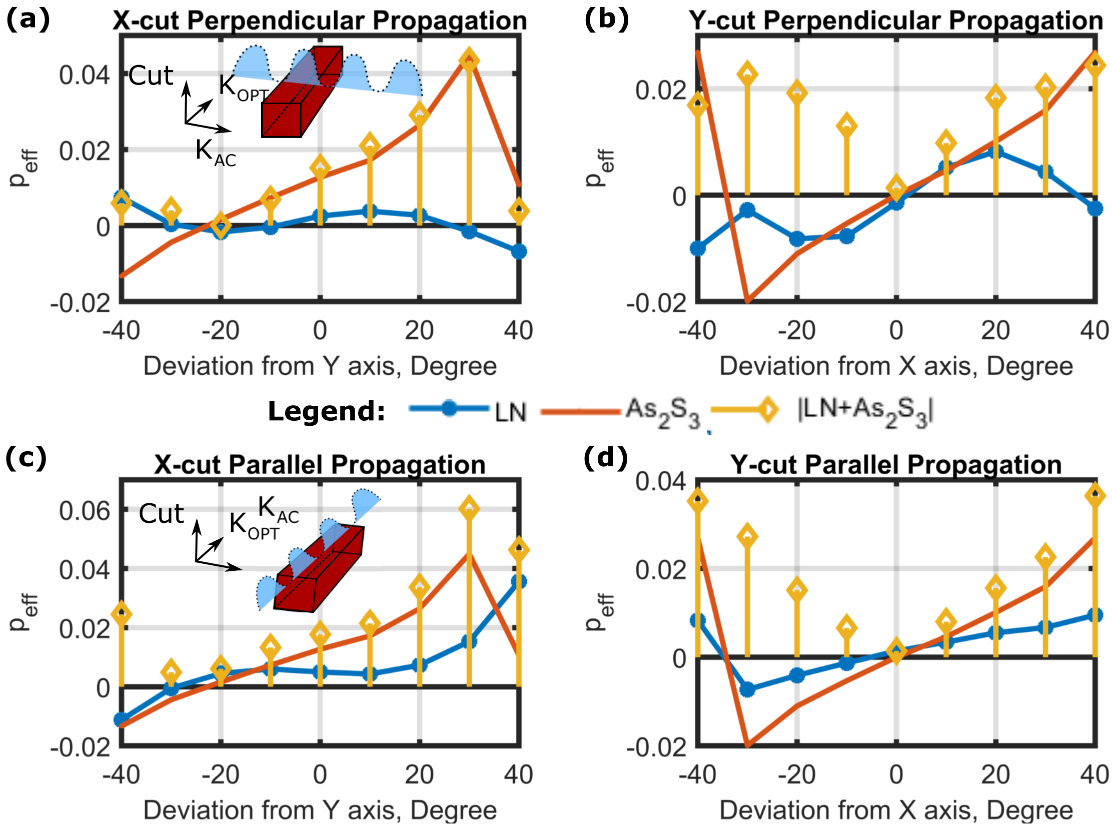

FIGURE 5.8: Effective acousto-optic coefficient calculated for perpendicular propagation in (a) X-cut and (b) Y-cut LNOI, and for parallel propagation in (c) X-cut and (d) Y-cut LNOI with As_2S_3 on top.

Fig. 5.8(a) and (b) shows the calculated effective AO coefficient for As_2S_3 and LN for perpendicular propagation setup. These values are represented with their signs which is determined by the strain phase, participating AO coefficients of LN and their relative amplitudes. The values for LN material coefficients are adopted from [57, 58]. Piezoelectric effects were taken into account for calculating the effective AO coefficients in LN which is thoroughly discussed in [53]. We have studied these coefficients for acoustic wave propagating in different directions on both X-cut and Y-cut LNOI. By comparing the p_{eff} values for both materials we can see that in some directions they are acting in phase, and in some directions they are acting out of phase with each other. For instance, in Fig. 5.8(a) for θ = -40^0, p_{eff} contribution from As_2S_3 and LN are opposite to each other. Whereas, for θ = 10^0 both coefficients have the same sign. Therefore, when we add up the contributions from both materials and look into their magnitude ($|p_{eff}^{LN}+p_{eff}^{As}|$), we can have a picture of overall p_{eff} of the hybrid material platform. Similarly, p_{eff} values are calculated for parallel propagation in both X-cut and Y-cut LNOI including As_2S_3 on top as depicted in Fig. 5.8(c) and (d).

5.2.3 Acousto-optic Properties of Hybrid Platform

The AO coefficients that we have calculated can be plugged into Eqn. 5.10, to determine the AOFOM for the hybrid material platform. Experimental measurements in Fig. 5.9 shows that average surface velocity for SH_0 propagation increases after depositing As_2S_3 on LNOI. Average surface acoustic velocity increase by the percentage of 1.68, 2.6 and 1.3 was recorded for SH_0 propagating along the direction deviated from y axis by -10^0, 0^0 and +10^0 respectively on X-cut LNOI. We made a simplified assumption that incorporating As_2S_3 with LNOI causes a velocity increases by 2% regardless of the LN anisotropy.

Based on this assumption, we have calculated M_2 for As_2S_3 on LNOI platform which is summarized in Fig. 5.10. The M_2 values are normalized to the M_2 value for SH_0 propagating along θ = 0^0 on LNOI. Fig. 5.10(a) shows that for perpendicular propagation on X-cut LNOI, addition of As_2S_3 can significantly enhance modulation properties for SH_0 propagating in between -10^0 and +30^0. Hybrid material structure also benefits when compared to Y-cut LNOI platform as in Fig.5.10(b).

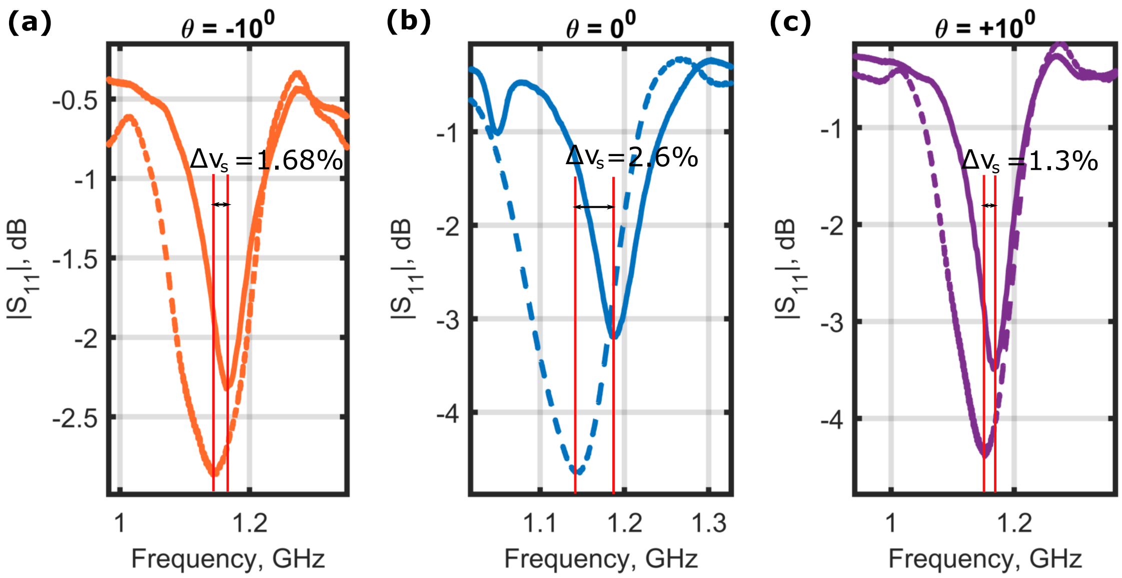

FIGURE 5.9: Surface velocity increase for SH_0 propagation after depositing As_2S_3 on top of LNOI. Here, dashed line represents frequency response before As_2S_3 deposition, and solid line represents response after As_2S_3 deposition. These frequency responses were measure for devices with Λ = 3.4 μm and SH_0 propagating on X-cut LNOI in directions deviated from y axis by an angle of (a) -10^0 (b) 0^0 (c) $+10^0$.

Even parallel propagation setup can also enjoy significant improvement using hybrid structure on both X-cut LNOI (Fig. 5.10(c)) and Y-cut LNOI (Fig. 5.10(d)). However, such improvements are more pronounced in case of Y-cut LNOI than X-cut LNOI if the hybrid structure is compared to its respective LNOI structure. But if we compare the overall performance in both cut of LNOI after the addition of As_2S_3 in this configuration, the magnitude of M_2 for both cuts would be comparable. It means addition of As_2S_3 on Y-cut LNOI makes it comparable to hybrid X-cut LNOI platform, whereas similar comparison between LNOI platforms alone would proclaim X-cut superior to Y-cut LNOI. These results and findings can provide useful information for choosing the cut of LN for specific application and provide insight into the extent of modulation enhancement possible using a hybrid structure over LNOI only structure.

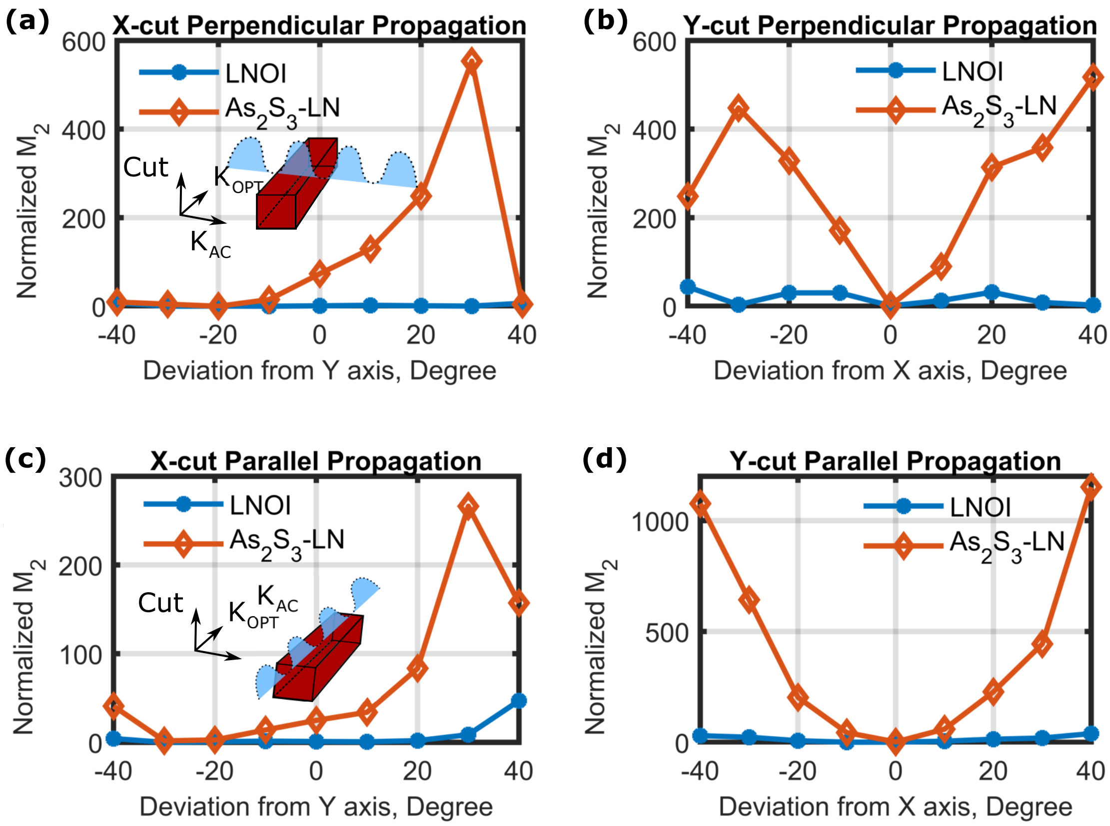

FIGURE 5.10: Acousto-optic figure of merit M_2 calculated for perpendicular propagation in (a) X-cut (normalized by $1.1\text{x}10^{-18}$ s/kg^3) and (b) Y-cut (normalized by $0.4\text{x}10^{-18}$ s/kg^3) LNOI, and for parallel propagation in (c) X-cut (normalized by $4.4\text{x}10^{-18}$ s/kg^3) and (d) Y-cut (normalized by $0.3\text{x}10^{-18}$ s/kg^3) LNOI with As_2S_3 on top.

For instance, in an optical phase modulation (perpendicular propagation) scheme on X-cut LNOI, maximum K_t^2 is achieved for θ = -10^0 (Fig. 4.4(e)). But M_2 for LNOI and hybrid platforms are quite similar in this direction. Whereas, if SH_0 propagation direction is chosen to be θ = +10^0, there will be a small reduction in K_t^2 requiring a minor enhancement in the acoustic device footprint for the impedance matching, but 100x improvement in the M_2 value is achieved for hybrid structure. Such improvement in M_2 can roughly be narrated as 10x improvement in the optical phase modulation per unit square root of acoustic power (assuming other device performance parameters are constant). Similar improvement can also be achieved for parallel propagation on X-cut LNOI hybrid structure, by choosing θ = +20^0 as SH$_0$ propapagation direction instead of choosing θ = -10^0. In this case, loss in K_t^2 would be higher (Fig. 4.4(e)), but for applications like beam steering, such acoustic device footprint enhancement due to the compensation for impedance mismatch may be considered as minor trade off given the achieved diffraction efficiency improvement.

5.2.4 Envisioned High Frequency Modulator

As in Fig. 5.11, our envisioned HF AOM device consists of IDTs launching propagating SH$_0$ wave, and optical RTR is used as the sensing mechanism to detect the phase modulation induced by the acousto-optic effect. To ensure push-pull operation, RTR arms are separated by an odd multiple of $\Lambda/2$.

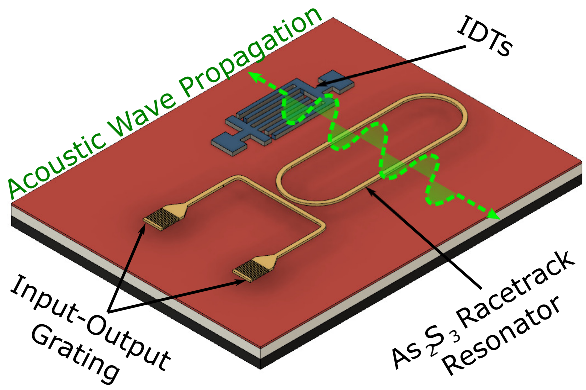

Figure 5.11: Schematic of the envisioned high frequency acousto-optic modulator.

Similar modulator device implementation has been demonstrated in [53] using RTR and acoustic resonator. Here, SH$_0$ is launched by applying alternating voltage signal to the IDTs, and optical VGA setup is used couple light into and from the photonic circuit.

Chapter 6

Conclusion and Future Work

6.1 Conclusion

Acoustic wave propagating in an optically transparent medium produces a periodic modulation of the refractive index of that medium through the acousto-optic effect. Such interaction can either be used in diffracting light or in manipulating the optical waveguiding medium to induce optical phase modulation. There are variety of applications where acousto-optic interaction can play significant role. Starting from microwave-to-optical conversion, acousto-optic platform could also find applications in optical comb generation, on-chip optical routing, optical mode conversion, stimulated Brillouin scattering, beam steering and many more. We have introduced As_2S_3 with LN to build a hybrid acousto-optic platform which promises some exciting features.

As As_2S_3 is a photosensitive material, we have addressed this issue and resolved the photodecomposition problem by using ~ 100nm thick SiO_2 cap layer, which prevents oxidation of the As_2S_3 film. We have experimentally verified that As_2S_3 can act as a hard mask during wet etch process using HF. These fabrication related information can be useful for future work on As_2S_3 processing.

Chapter 3 summarizes the photonic components built on the As_2S_3 film. One dimensional grating coupler is demonstrated which offers -3dB coupling efficiency. This is the best reported grating coupler on the As_2S_3 on oxide on LN material platform till date for vertical coupling. Besides, optical waveguide loss is extracted using optical RTR. Thermal coefficients for optical waveguides on LNOI, As_2S_3 on LNOI and As_2S_3 on bulk LN has been extracted for the first time using optical RTR. This thermal coefficient represents both thermo-optic effect and thermal expansion effect.

Acoustic wave generation in both bulk LN and LNOI platform are thoroughly discussed in chapter 4. For LF operation, Ralyleigh SAWs are used as the acoustic excitation. Since, the goal is to integrate As_2S_3 on bulk LN keeping an oxide cladding layer between the two materials, long SAW wavelength allows strong strain interaction inside the As_2S_3 thin film sitting on top of the oxide layer. The LF acoustic device consists of a SAW cavity with IDTs and acoustic reflector gratings, which is developed for the acousto-optic gyroscope demonstration. For the high frequency acoustic device, shear horizontal (SH_0) wave is chosen as the acoustic mode for it offers high electromechanical coupling coefficient in ~GHz frequency range of operation as well as offers higher speed enabling slightly higher frequency of operation compared to the SAW mode, which offers very poor electromechanical coupling (below 2%). Implementation of high frequency IDTs has been demonstrated on X-cut LNOI for SH_0 propagating along y-direction and in directions deviated from y-axis in either direction by 10^0. Experimental measurements shows agreement with the predicted high electromechanical coupling (~ 20%).

Integration of acoustic device and photonic devices are presented in chapter 5. The LF AOM is formed by an As_2S_3 MZI, operating in a push-pull configuration and placed inside a SAW cavity on a Y-cut LN wafer. This is the first demonstration of such AOM in this As_2S_3 on oxide on LN platform. In this approach, the high index contrast of As_2S_3 waveguides is exploited to attain a high optical confinement. Additionally, the placement of the photonic MZI inside the SAW cavity enhances the AO interaction due to the high quality factor (Q) of the SAW resonator. An analytical expression that describes such enhancement as a function of the AO coefficient of As_2S_3 is derived in conjunction with COMSOL finite element methods to describe strain in the SAW cavity. By fitting this expression to experimental data, the AO coefficient (p_{11} and p_{12}, where $p_{11} \approx p_{12}$) for As_2S_3 is extracted to be 0.29 at the wavelength of 1550 nm. This is the first time that the AO coefficient of thin film As_2S_3 is experimentally derived. Given the isotropic nature of As_2S_3, it also decouples the design of the acoustic device from the photonic components, increasing flexibility in the demonstration of advanced AOMs.

While we have experimental demonstration of AOM for LF application, we have envisioned implementing HF modulator using propagating SH_0 wave generated by IDTs and optical phase modulation induced in push-pull mode by an optical RTR. Even though such modulator has not been experimentally demonstrated, all the key components (i.e. IDTs, grating couplers, resonators) required for such demonstration are experimentally verified. We have a qualitative study of the LNOI platform and the benefit of adding As_2S_3 on it in order to the enhance modulation efficiency of the material platform.

6.2 Future Work

Implementation of the HF AOM would allow extraction of the effective AO coefficient of the As_2S_3-LN hybrid waveguides in different orientation. Extraction of AO coefficient would further validate the qualitative analysis presented in the section 5.2.

Besides, LF AOM performance can be significantly enhanced by implementing efficient grating coupler design presented in chapter 3, improving the waveguide propagation loss using the sonication method at the resist strip step as mentioned in the section 3.3. The MMI coupler design can also be optimized. All these modifications can approximately improve the modulated output power by 17dB.

Operating frequency for the HF AOM would be another promising route to pursue. Both thinner LN and As_2S_3 film would be required for such demonstration, to ensure equal propagating optical power confinement within both the mediums. Nanoscale acoustic resonator structure can be used to enhance the AO interaction utilizing the acoustic Q-factor.

Large AO coefficient has been demonstrated in eitaxial $PbTiO_3$ films [59] which seems superior to both LN and As_2S_3 in terms of refractive index and magnitude of AO coefficients. It would be interesting to study the strain interaction in this material platform to understand its effective AO coefficient, effect of incorporating As_2S_3 with this new material platform.

Bibliography

[1] Matthieu Roussey et al. 'Experimental and theoretical characterization of a lithium niobate photonic crystal'. In: *Applied Physics Letters* 87.24 (2005), p. 241101.

[2] M Roussey et al. 'Electro-optic effect exaltation on lithium niobate photonic crystals due to slow photons'. In: *Applied physics letters* 89.24 (2006), p. 241110.

[3] M Diwekar et al. 'Optical and magneto-optical studies of two-dimensional metallodielectric photonic crystals on cobalt films'. In: *Applied physics letters* 84.16 (2004), pp. 3112–3114.

[4] Lanlan Gu et al. 'High speed silicon photonic crystal waveguide modulator for low voltage operation'. In: *Applied physics letters* 90.7 (2007), p. 071105.

[5] Edilson A Camargo, Harold MH Chong and M Richard. '2D photonic crystal thermo-optic switch based on AlGaAs/GaAs epitaxial structure'. In: *Optics Express* 12.4 (2004), pp. 588–592.

[6] Mohamed Mahmoud et al. 'Novel on chip rotation detection based on the acousto-optic effect in surface acoustic wave gyroscopes'. In: *Optics Express* 26.19 (2018), pp. 25060–25075.

[7] Semere Ayalew Tadesse and Mo Li. 'Sub-optical wavelength acoustic wave modulation of integrated photonic resonators at microwave frequencies'. In: *Nature communications* 5 (2014), p. 5402.

[8] Krishna C Balram et al. 'Coherent coupling between radiofrequency, optical and acoustic waves in piezo-optomechanical circuits'. In: *Nature photonics* 10.5 (2016), p. 346.

[9] IC Chang. 'Acoustooptic devices and applications'. In: *IEEE transactions on sonics and ultrasonics* 23.1 (1976), p2.

[10] MSI Khan et al. 'Acousto-Optic Modulator based on the Integration of Arsenic Trisulfide Photonic Components with Lithium Niobate Surface Acoustic Waves'. In: *Conference on Lasers and Electro-Optics*. Optical Society of America, 2019, SF3N.4. DOI: 10.1364/CLEO_SI.2019.SF3N.4. URL: http://www.osapublishing.org/abstract.cfm?URI=CLEO_SI-2019-SF3N.4.

[11] SJ Ben Yoo, Binbin Guan and Ryan P Scott. 'Heterogeneous 2D/3D photonic integrated microsystems'. In: *Microsystems & Nanoengineering* 2 (2016), p. 16030.

[12] Linbo Shao et al. 'Microwave-to-optical conversion using lithium niobate thin-film acoustic resonators'. In: *Optica* 6.12 (2019), pp. 1498–1505.

[13] Donggyu B Sohn and Gaurav Bahl. 'Direction reconfigurable nonreciprocal acousto-optic modulator on chip'. In: *APL Photonics* 4.12 (2019), p. 126103.

[14] Ravi Pant et al. 'On-chip stimulated Brillouin scattering'. In: *Optics express* 19.9 (2011), pp. 8285–8290.

[15] John S Berkes, Samuel W Ing Jr and William J Hillegas. 'Photodecomposition of amorphous As2Se3 and As2S3'. In: *Journal of Applied Physics* 42.12 (1971), pp. 4908–4916.

[16] Duk-Yong Choi et al. 'SU-8 protective layer in photo-resist patterning on As2S3 film'. In: *physica status solidi c* 8.11-12 (2011), pp. 3183–3186.

[17] Ashraf Mahmoud et al. 'Acousto-Optic Gyroscope with Improved Sensitivity and 100 second Stability in a Small Form Factor'. In: *2019 IEEE International Symposium on Inertial Sensors and Systems (INERTIAL)*. IEEE. 2019, pp. 1–4.

[18] Supriyo Datta. *Surface acoustic wave devices*. Prentice Hall, 1986.

[19] MSI Khan, James A Bain and Gianluca Piazza. 'Efficient arsenic trisulfide vertical grating coupler on lithium niobate for integrated photonic applications'. In: *Optics letters* 44.18 (2019), pp. 4558–4561.

[20] Attila Mekis et al. 'A grating-coupler-enabled CMOS photonics platform'. In: *IEEE Journal of Selected Topics in Quantum Electronics* 17.3 (2011), pp. 597–608.

[21] Blair Morrison et al. 'Compact Brillouin devices through hybrid integration on silicon'. In: *Optica* 4.8 (2017), pp. 847–854.

[22] Chen Zhang and CK Madsen. 'Demonstration of an As2S3-on-LiNbO3 grating coupler and its application of measuring a grating-based filter'. In: *IEEE Photonics Journal* 8.6 (2016), pp. 1–7.

[23] C Alonso-Ramos et al. 'Efficient fiber-to-chip grating coupler for micrometric SOI rib waveguides'. In: *Optics Express* 18.14 (2010), pp. 15189–15200.

[24] Neil Na et al. 'Efficient broadband silicon-on-insulator grating coupler with low backreflection'. In: *Optics letters* 36.11 (2011), pp. 2101–2103.

[25] Xia Chen, Chao Li and Hon Ki Tsang. 'Fabrication-tolerant waveguide chirped grating coupler for coupling to a perfectly vertical optical fiber'. In: *IEEE Photonics Technology Letters* 20.23 (2008), pp. 1914–1916.

[26] Diedrik Vermeulen et al. 'High-efficiency fiber-to-chip grating couplers realized using an advanced CMOS-compatible silicon-on-insulator platform'. In: *Optics express* 18.17 (2010), pp. 18278–18283.

[27] Wim Bogaerts, Peter De Heyn et al. *Silicon microring resonators. Laser Photonics Reviews*. 2011.

[28] William J Tropf, Michael E Thomas and Terry J Harris. 'Properties of crystals and glasses'. In: *Handbook of optics* 2 (1995), pp. 33–61.

[29] Jiro Matsuda. 'Studies on Arsenic Trisulfide Glass'. In: *Bulletin of the Chemical Society of Japan* 33.2 (1960), pp. 208–211.

[30] Richard M White and Fred W Voltmer. 'Direct piezoelectric coupling to surface elastic waves'. In: *Applied physics letters* 7.12 (1965), pp. 314–316.

[31] Kenji Uchino. *Advanced piezoelectric materials: Science and technology*. Woodhead Publishing, 2017.

[32] BA Auld. 'Rayleigh wave propagation'. In: *Rayleigh-Wave Theory and Application*. Springer, 1985, pp. 12–28.

[33] Ashraf Mahmoud. 'Toward Navigation Grade Acousto-Optic Gyroscope'. PhD thesis. Carnegie Mellon University, 2020.

[34] CK Campbell. 'Obtaining the fundamental and harmonic radiation conductances of a reflective SAW interdigital transducer'. In: *1998 IEEE Ultrasonics Symposium. Proceedings (Cat. No. 98CH36102)*. Vol. 1. IEEE. 1998, pp. 169–173.

[35] Ken-ya Hashimoto and Ken-Ya Hashimoto. *Surface acoustic wave devices in telecommunications*. Springer, 2000.

[36] Nils T Otterstrom et al. 'Resonantly enhanced nonreciprocal silicon Brillouin amplifier'. In: *Optica* 6.9 (2019), pp. 1117–1123.

[37] Jiyang Ma et al. 'Chip-Based Optical Isolator and Nonreciprocal Parity-Time Symmetry Induced by Stimulated Brillouin Scattering'. In: *Laser & Photonics Reviews* 14.5 (2020), p. 1900278.

[38] Donggyu B Sohn, Seunghwi Kim and Gaurav Bahl. 'Time-reversal symmetry breaking with acoustic pumping of nanophotonic circuits'. In: *Nature Photonics* 12.2 (2018), pp. 91–97.

[39] Freek Ruesink et al. 'Nonreciprocity and magnetic-free isolation based on optomechanical interactions'. In: *Nature communications* 7.1 (2016), pp. 1–8.

[40] JunHwan Kim et al. 'Non-reciprocal Brillouin scattering induced transparency'. In: *Nature Physics* 11.3 (2015), pp. 275–280.

[41] Chun-Hua Dong et al. 'Brillouin-scattering-induced transparency and non-reciprocal light storage'. In: *Nature communications* 6.1 (2015), pp. 1–6.

[42] Eric A Kittlaus et al. 'Non-reciprocal interband Brillouin modulation'. In: *Nature Photonics* 12.10 (2018), pp. 613–619.

[43] Ravi Pant et al. 'On-chip stimulated Brillouin Scattering for microwave signal processing and generation'. In: *Laser & Photonics Reviews* 8.5 (2014), pp. 653–666.

[44] Weiwei Zhang and Robert A Minasian. 'Widely tunable single-passband microwave photonic filter based on stimulated Brillouin scattering'. In: *IEEE Photonics Technology Letters* 23.23 (2011), pp. 1775–1777.

[45] David Marpaung et al. 'Low-power, chip-based stimulated Brillouin scattering microwave photonic filter with ultrahigh selectivity'. In: *Optica* 2.2 (2015), pp. 76–83.

[46] Mattia Pagani et al. 'Tunable wideband microwave photonic phase shifter using on-chip stimulated Brillouin scattering'. In: *Optics express* 22.23 (2014), pp. 28810–28818.

[47] David Kwong et al. 'On-chip silicon optical phased array for two-dimensional beam steering'. In: *Optics letters* 39.4 (2014), pp. 941–944.

[48] Tsutomu Takai et al. 'High-performance SAW resonator on new multilayered substrate using LiTaO 3 crystal'. In: *IEEE transactions on ultrasonics, ferroelectrics, and frequency control* 64.9 (2017), pp. 1382–1389.

[49] Iren E Kuznetsova et al. 'Investigation of acoustic waves in thin plates of lithium niobate and lithium tantalate'. In: *IEEE Transactions on Ultrasonics, Ferroelectrics, and Frequency Control* 48.1 (2001), pp. 322–328.

[50] RW Dixon. 'Photoelastic properties of selected materials and their relevance for applications to acoustic light modulators and scanners'. In: *Journal of Applied Physics* 38.13 (1967), pp. 5149–5153.

[51] Jieping Xu and Robert Stroud. *Acousto-optic devices: principles, design, and applications*. Vol. 12. Wiley-Interscience, 1992.

[52] Larry A Coldren, Scott W Corzine and Milan L Mashanovitch. *Diode lasers and photonic integrated circuits*. Vol. 218. John Wiley & Sons, 2012.

[53] Lutong Cai et al. 'Acousto-optical modulation of thin film lithium niobate waveguide devices'. In: *Photonics Research* 7.9 (2019), pp. 1003–1013.

[54] MSI Khan et al. 'Acousto-Optic Modulator based on the Integration of Arsenic Trisulfide Photonic Components with Lithium Niobate Surface Acoustic Waves'. In: *CLEO: Science and Innovations*. Optical Society of America. 2019, SF3N–4.

[55] Antonio Crespo-Poveda et al. 'Synchronized photonic modulators driven by surface acoustic waves'. In: *Optics express* 21.18 (2013), pp. 21669–21676.

[56] Md Shofiqul Islam Khan et al. 'Extraction of Elastooptic Coefficient of Thin-Film Arsenic Trisulfide Using a Mach–Zehnder Acoustooptic

Modulator on Lithium Niobate'. In: *Journal of Lightwave Technology* 38.7 (2020), pp. 2053–2059.

[57] Jieping Xu and Robert Stroud. *Acousto-optic devices: principles, design, and applications*. Vol. 12. Wiley-Interscience, 1992.

[58] RS Weis and TK Gaylord. 'Lithium niobate: summary of physical properties and crystal structure'. In: *Applied Physics A* 37.4 (1985), pp. 191–203.

[59] Lan Chen et al. 'Large elasto-optic effect in epitaxial PbTiO 3 films'. In: *Physical review letters* 115.26 (2015), p. 267602.

[60] Andrés Sosa Andrade. 'Design of a silicon photonic multimode interference coupler'. In: (2012).

Appendix A

For a single input, the field distribution at distance z inside the MMI coupler can be written as the superposition of all guided modes:

$$\Psi(x,z) = \sum_{\nu=0}^{m-1} C_\nu \Phi_\nu(x) \exp\left(j\frac{\nu(\nu+2)\pi}{3L_\pi}z\right) \tag{.1}$$

where ν is the mode number, Φ is the modal field distribution within the MMI coupler, $L_\pi (= 4nW_e^2/3\lambda)$ the beat length for the two lowest order modes and C_ν the field excitation coefficient [60], which could be written as:

$$C_\nu = \frac{\int \Psi(x,0)\Phi_\nu(x)}{\sqrt{\int \Phi_\nu^2(x)}} \tag{.2}$$

Here $\Psi(x,0)$ is assumed to be a single mode input from the wire waveguide. For one of the output waveguides at a distance $z = L = L_\pi/2$ the field distribution becomes

$$\Psi(x,L) = \sum_{\nu=0}^{m-1} C_\nu \Phi_\nu(x) \exp\left(j\nu(\nu+2)\frac{\pi}{6}\right) \tag{.3}$$

Since the output field is the superposition of the two input fields, it can be written as follows

$$\begin{aligned}\Psi(x,L) = &\sum_{\nu=0}^{m-1} C_\nu \Phi_\nu(x) \exp\left(j\nu(\nu+2)\frac{\pi}{6}+\delta_1\right)+\\ &(-1)^\nu \sum_{\nu=0}^{m-1} C_\nu \Phi_\nu(x) \exp\left(j\nu(\nu+2)\frac{\pi}{6}+\delta_2\right)\end{aligned}$$

where $\delta_1 = -\theta_{AO}+\theta_{MZI1}$ and $\delta_2 = \theta_{AO}+\theta_{MZI2}+\theta_{MMI}$ represent the phases at the output ports for two different inputs, which include phase changes induced by the MZI arm lengths, θ_{MZI1} and θ_{MZI2}, AO modulation, θ_{AO}, and path difference within MMI, θ_{MMI}.

Since the optical power $H \propto I \propto \Psi^2$, we can write the output power as

$$\begin{aligned}H_{out} &= H_{even}\cos^2\left(\frac{\delta_2-\delta_1}{2}\right) + H_{odd}\sin^2\left(\frac{\delta_2-\delta_1}{2}\right)\\ &= const. + \frac{1}{2}H_{sub}\{\cos\left(\alpha_p\sqrt{P_e}\cos(\Omega_m t)\right)\cos\theta_0\\ &\qquad - \sin\left(\alpha_p\sqrt{P_e}\cos(\Omega_m t)\right)\sin\theta_0\}\end{aligned}$$

Here, optical power $H_{sub} = H_{even} - H_{odd}$ (H_{even} related to the power for the even modes and H_{odd} related to the power for the odd modes) and phase due to fabrication error in MZI arms is $\Delta\theta_{MZI} = \theta_{MZI2} - \theta_{MZI1}$ (θ_{MZI1} and θ_{MZI2} are the phases introduced at the two MMI input ports). AO phase modulation due to the SAW wave (both arms) can be expressed as, $2\theta_{AO} = \alpha_p \sqrt{P_e} \cos(\Omega_m t)$ where and $\theta_0 = \Delta\theta_{MZI} + \theta_{MMI}$.